



HAL
open science

Low-Mach correction for Lagrangian acoustic Riemann solvers on unstructured meshes

Emmanuel Labourasse

► **To cite this version:**

Emmanuel Labourasse. Low-Mach correction for Lagrangian acoustic Riemann solvers on unstructured meshes. 2017. hal-01584308v1

HAL Id: hal-01584308

<https://hal.science/hal-01584308v1>

Preprint submitted on 8 Sep 2017 (v1), last revised 26 Mar 2018 (v2)

HAL is a multi-disciplinary open access archive for the deposit and dissemination of scientific research documents, whether they are published or not. The documents may come from teaching and research institutions in France or abroad, or from public or private research centers.

L'archive ouverte pluridisciplinaire **HAL**, est destinée au dépôt et à la diffusion de documents scientifiques de niveau recherche, publiés ou non, émanant des établissements d'enseignement et de recherche français ou étrangers, des laboratoires publics ou privés.

Low-Mach correction for Lagrangian acoustic Riemann solvers on unstructured meshes

E. Labourasse^{a,*}

^aCEA, DAM, DIF, F-91297 ARPAJON, FRANCE.

Abstract

We propose a low-Mach correction for cell-centered schemes in Lagrangian frame. After transposing some classical results in Eulerian frame to Lagrangian frame, we show why classical cell-centered schemes in Lagrangian frame are not able to capture the low-Mach regime except by using unreasonably fine meshes. Consequently, we propose a slight modification of the original scheme, which is easy to implement in any scheme using a acoustic Godunov Riemann solver on unstructured mesh, and is costless in term of CPU time. We demonstrate that this modification cures this flaw. The properties of the original semi-discrete scheme (consistence, conservation) are preserved. Particular attention is paid to the entropy condition, proving its compatibility with the modification proposed. We assess this new scheme on several low and high-Mach problems, to demonstrate its good behaviour in all regimes. Last test problem is devoted to the study of the growth rate of instability in convergent configuration. It shows that even if the problem is globally very compressible, the low-Mach correction can have a significant impact on the solution.

Keywords: Lagrangian hydrodynamics, compressible flows, Euler equations, low-Mach regime, Finite Volumes

1. Introduction

Since 1950 and the seminal work of Von Neumann and Richtmyer [41], semi-Lagrangian methods are popular for the calculation of high velocity gaz dynamics (refer to [3, 5, 34] and references therein for more details about these methods). This popularity with respect to Eulerian methods is partly due to the fact, that the convection terms are not taken into account in the fluxes, but implicitly by the mesh motion. The original scheme of Von Neumann and Richtmyer is said to be «staggered in space», what means that the velocity's unknowns are associated to the vertices of the cells, while the thermodynamic's

*Corresponding author

Email address: `emmanuel.labourasse@cea.fr` (E. Labourasse)

unknowns (internal energy, density) are associated to the cells of the mesh. This is a natural choice for semi-Lagrangian methods, because it directly provides a procedure to move the mesh compatibly with the velocity unknowns. This intrinsic quality justifies the great number of works devoted to this method for more than 60 years. Among these works, some concern the design of artificial viscosity. Artificial viscosity is needed in staggered schemes, because the discretization of the pressure gradient is by construction "centered" and does not account for the entropy increase in shock waves. The artificial viscosity cures this flaw in adding a dissipative term proportional to the velocity jump into the momentum equation. Modern versions of this mechanism include a monotonic second-order reconstruction of this jump, in order to discard the artificial viscosity for regular (isentropic) flows. One indirect and never mentioned consequence of this enhancement is to widely improve the behaviour of staggered schemes in low-Mach regimes. Indeed, it has been shown that a correct calculation of low-Mach flows is directly related to a centered pressure gradient (refer for instance to [18]).

Finite-Volume «cell-centered» (or colocated) schemes are the alternative to the former «staggered» schemes. At the contrary to «staggered» schemes, all the unknowns of these schemes, including the velocity, are mean values associated to the cells of the mesh. The main advantage of this configuration, is that it greatly facilitates the balance of momentum and total energy, making in particular much more easier its extension to Arbitrary Lagrange Euler (ALE). However, since the velocity unknowns are no more associated to the vertices, one needs an extra ingredient to predict the mesh motion. Recent works [22, 36] have successfully overcome this difficulty, in solving the acoustic Riemann problem at the vertices instead of the sides of the cells (as done in the first attempts [1]). Numerous variants of these schemes (refer among other to [9, 8, 13, 23, 33]) have been recently developed. All use an acoustic Godunov solver to compute the fluxes. A peculiar feature of this solver, is that it enforces by construction an entropy deposit, in including a term proportional to the velocity jump into the pressure gradient. This feature makes these schemes not well suited to capture the low-Mach regime, what have been previously experienced in the Eulerian community. Godunov solvers are widely used in the Eulerian community, and many works have been devoted to this issue (refer for instance to [6, 10, 11, 15, 16, 17, 18, 19, 25, 30, 31, 32, 40, 45, 47]), mainly for Cartesian grids. Only few works are dealing with unstructured meshes, and none of them in Lagrangian frame (however Chalons *et al* [10, 11] consider a Lagrange + remap method to solve the equations in the Eulerian frame). Dellacherie [18] has enlighten the specificity of the low-Mach problem for multi-dimensional schemes, and explains why successful mono-dimensional scheme can fail in multi-D.

In this paper we propose a low-Mach correction for cell-centered schemes in Lagrangian frame. After transposing some classical results in Eulerian frame to Lagrangian frame in section 2, we show why classical cell-centered schemes are not able to capture the low-Mach regime in section 3. Then in section 4, we propose a slight modification of the original scheme, which is easy to implement in any scheme using a acoustic Godunov Riemann solver on unstructured mesh,

and is costless in term of CPU time. We demonstrate that this modification cures this flaw. The properties of the original semi-discrete scheme (consistence, conservation) are preserved. We devote the section 5 to the entropy condition, proving its compatibility with the modification proposed. We give usefull implementation details in section 6. Finally, we assess in section 7, this new scheme on several low and high-Mach problems, to demonstrate its good behaviour in all regimes. Last test problem is devoted to the study of the growth rate of instability in convergent configuration. It shows that even if the problem is globally very compressible, the low-Mach correction can have a significant impact on the solution.

2. Framework and notations

This preliminary section is devoted to the specification of the framework and notation used in the remainder of the paper.

2.1. Governing equations and low-Mach regime

We consider the semi-lagrangian form of the Euler system of conservation laws:

$$\begin{cases} \rho D_t \tau - \nabla \cdot \mathbf{u} = 0 & \text{volume,} \\ \rho D_t \mathbf{u} + \nabla p = \mathbf{0} & \text{momentum,} \\ \rho D_t e + \nabla \cdot (p\mathbf{u}) = 0 & \text{total energy} \end{cases} \quad (1)$$

where $D_t(\varphi) := (\partial_t + \mathbf{u} \cdot \nabla)\varphi$ is the Lagrangian derivative, ρ is the density, $\tau = 1/\rho$ is the specific volume, \mathbf{u} is the velocity, p is the pressure, $e = \varepsilon + \mathbf{u}^2/2$ the specific total energy and ε the specific internal energy.

This set of equation is supplemented by an equation of state $p = p(\rho, \varepsilon)$ and endowed with an entropy evolution law

$$\rho D_t \eta \geq 0 \quad (2)$$

where η is the physical entropy fulfilling the Gibbs relation

$$T d\eta = d\varepsilon + p d\tau. \quad (3)$$

where T is the temperature.

In the following, we are interested in the low-Mach regime corresponding to $M = |\mathbf{u}|/c \ll 1$, with $c = \sqrt{\left. \frac{\partial p}{\partial \rho} \right|_{\eta}}$ the sound-speed. In order to study this regime, we rescale the system (1) using a set of non-dimensional variables:

$$\bar{\mathbf{x}} = \frac{\mathbf{x}}{L}, \quad \bar{t} = \frac{t}{t_R}, \quad \bar{\rho} = \frac{\rho}{\rho_R}, \quad \bar{p} = \frac{p}{p_R}, \quad \bar{\mathbf{u}} = \frac{\mathbf{u}}{u_R}, \quad \bar{e} = \frac{e}{e_R}, \quad \bar{c} = \frac{c}{c_R} \quad (4)$$

where the parameters $L, t_R, \rho_R, p_R, u_R = L/t_R, e_R = p_R \rho_R$ and $c_R = \sqrt{p_R/\rho_R}$ denote respectively a characteristic length, time, density, pressure, velocity, energy and sound-speed, and $\mathbf{x} \in \mathbb{R}^d$ is the position. The characteristic Mach number is defined as $M = u_R/c_R$, and the system (1) recasts:

$$\begin{cases} \bar{\rho} \bar{D}_{\bar{t}} \bar{\tau} - \bar{\nabla} \cdot \bar{\mathbf{u}} = 0 & \text{volume,} \\ \bar{\rho} \bar{D}_{\bar{t}} \bar{\mathbf{u}} + \frac{1}{M^2} \bar{\nabla} \bar{p} = \mathbf{0} & \text{momentum,} \\ \bar{\rho} \bar{D}_{\bar{t}} \bar{e} + \bar{\nabla} \cdot (\bar{p} \bar{\mathbf{u}}) = 0 & \text{total energy} \end{cases} \quad (5)$$

with $\bar{e} = \bar{\varepsilon} + M^2 \bar{\mathbf{u}}^2/2$, and $\bar{D}_{\bar{t}} \varphi := \partial_{\bar{t}} \varphi + \bar{\mathbf{u}} \cdot \bar{\nabla} \varphi$. **To lighten the notation we omit in the following the bar on the differential operators in the adimensionnal equations.**

To study the asymptotic low-Mach regime of the previous system, we perform a Hilbert expansion of all the variables with respect to the small parameter M ($\varphi = \varphi_0 + M\varphi_1 + M^2\varphi_2 + \dots$). Injecting it into the momentum equation of the system (5), we obtain $\nabla \bar{p}_0 = \nabla \bar{p}_1 = 0$. Consequently, $\bar{p}(\bar{\mathbf{x}}, \bar{t}) = \bar{p}_0(\bar{t}) + M^2 \bar{p}_2(\bar{\mathbf{x}}, \bar{t})$ and taking only the $\mathcal{O}(1)$ terms into (5), we get

$$\begin{cases} \bar{\rho}_0 D_t^0 \bar{\tau}_0 - \nabla \cdot \bar{\mathbf{u}}_0 = 0 & \text{volume,} \\ \bar{\rho}_0 D_t^0 \bar{\mathbf{u}}_0 + \nabla \bar{p}_2 = \mathbf{0} & \text{momentum,} \\ \bar{\rho}_0 D_t^0 \bar{\varepsilon}_0 + \bar{p}_0 \nabla \cdot (\bar{\mathbf{u}}_0) = 0 & \text{total energy.} \end{cases} \quad (6)$$

where $D_t^0 \bullet = \partial_t \bullet + \mathbf{u}_0 \cdot \nabla \bullet$.

The total energy conservation law has been changed into an internal energy balance law, equivalent to the conservation of the entropy, $D_t^0 \bar{\eta}_0 = 0$ (see equation (3)). Expanding the energy equation to the next order gives:

$$\bar{\rho}_0 D_t^0 \bar{\varepsilon}_1 + \bar{\rho}_1 D_t^0 \bar{\varepsilon}_0 + \bar{\rho}_0 \bar{\mathbf{u}}_1 \cdot \nabla \bar{\varepsilon}_0 + p_0 \nabla \cdot (\bar{\mathbf{u}}_1) = 0. \quad (7)$$

It means that $\bar{D}_t \bar{\eta}_1 = 0$, and then $\bar{D}_t \bar{\eta} = \mathcal{O}(M^2)$.

The previous analysis is formal. For a rigorous study of the low-mach regime, we refer the reader to the founding works of Klainerman and Majda [28, 29].

2.2. Notations

We have chosen a formalism general enough to express at once Glace [22], Eucclhyd [36] and CCH [8]. In this formalism, we denote the cells Ω_j , paving the computational domain Ω with the index j . The vertices of the mesh are denoted by the index r and the faces (or edges) by f . For instance, \mathbf{x}_j , \mathbf{x}_r and \mathbf{x}_f are the positions respectively of the center of cell j , the vertex r , and the middle of face f , as depicted on figure (1).

In the following, some quantities are defined relatively to the cell j , the node r or the face f . They are referred respectively as φ_j , φ_r or φ_f . Some quantities, as for instance the vectors \mathbf{N}_{jrf} and \mathbf{C}_{jr} of figure (1), can depend on two or even three different types of elements. The vector $\mathbf{N}_{jrf} = N_{jrf} \mathbf{n}_{jrf}$ is the outward directed surface normal to the face f owning the vertex r of the cell j , \mathbf{n}_{jrf} and N_{jrf} being respectively the unit normal vector and the half length corresponding to this face. In the following, we call \mathcal{J} the set of the cells, \mathcal{R} the set of the vertices, and \mathcal{F} the set of the faces (or edges) of the calculation domain. Consequently, we define \mathcal{F}_j the set of faces of the cell j , and \mathcal{F}_r the set of faces owning the vertex r . Similarly, \mathcal{R}_j and \mathcal{R}_f denote respectively the set of vertices of the cell j or of the face f , and \mathcal{J}_r and \mathcal{J}_f respectively the set

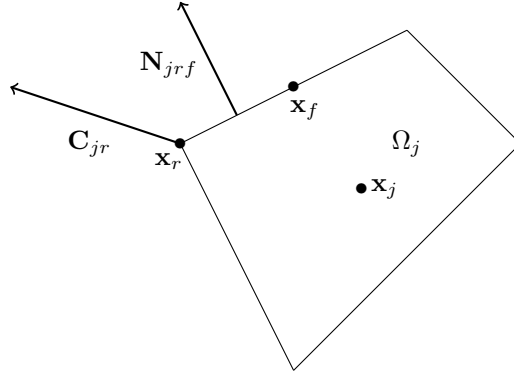


Figure 1: Notations

of cells owning the vertex r or the face f . We also make use of the notation \mathcal{J}_j , with j a cell index, to design all cells sharing a vertex with cell Ω_j . Finally, we condensate the intersection of the sets, for instance: $\mathcal{F}_{jr} := \mathcal{F}_r \cap \mathcal{F}_j$. To lighten the notations, we adopt the following conventions for sums: if no set is defined in the sum, it means that this set is **implicitly** defined by the indices of the quantities involved. For instance

$$\begin{aligned}
 \psi_j &= \sum_r \varphi_r & \text{means} & & \forall j \in \mathcal{J}, \quad \psi_j &= \sum_{r \in \mathcal{R}_j} \varphi_r \\
 \psi_r &= \sum_j \sum_f \varphi_{jf} & \text{means} & & \forall r \in \mathcal{R}, \quad \psi_r &= \sum_{j \in \mathcal{J}_r} \sum_{f \in \mathcal{F}_r \cap \mathcal{F}_j} \varphi_{jf} \\
 & & \text{or equivalently} & & \forall r \in \mathcal{R}, \quad \psi_r &= \sum_{f \in \mathcal{F}_r} \sum_{j \in \mathcal{J}_r \cap \mathcal{J}_f} \varphi_{jf} \\
 \psi_{jr} &= \sum_f \varphi_{jf} & \text{means} & & \forall r \in \mathcal{R}, \forall j \in \mathcal{J}_r, \quad \psi_{jr} &= \sum_{f \in \mathcal{F}_{jr}} \varphi_{jf} \\
 & & \text{or equivalently} & & \forall j \in \mathcal{J}, \forall r \in \mathcal{R}_j, \quad \psi_{jr} &= \sum_{f \in \mathcal{F}_{jr}} \varphi_{jf}
 \end{aligned}$$

The geometrical vector \mathbf{C}_{jr} is defined as

$$\forall r, \forall j, \quad \mathbf{C}_{jr} = \nabla_{\mathbf{x}_r} |\Omega_j| \tag{8}$$

Finally, we recall the geometrical identities, widely used in the following:

$$\left\{ \begin{array}{l} \forall j, \sum_r \mathbf{C}_{jr} = \mathbf{0}, \quad \forall r, \sum_j \mathbf{C}_{jr} = \mathbf{0}, \\ \forall j, \sum_r \sum_f \mathbf{N}_{jrf} = \mathbf{0}, \quad \forall r, \sum_j \sum_f \mathbf{N}_{jrf} = \mathbf{0}, \\ \forall r, \forall j, \sum_f \mathbf{N}_{jrf} = \mathbf{C}_{jr} \end{array} \right. \quad (9)$$

2.3. Semi-discrete conservation laws

With this formalism, the semi-discrete Glace [22], Eucclhyd [36] and CCH [8] schemes for Euler system (1) write

$$\left\{ \begin{array}{l} d_t \int_j 1 = \sum_r \mathbf{C}_{jr} \cdot \mathbf{u}_r \quad \text{volume,} \\ d_t \int_j \rho \mathbf{u} = - \sum_r \sum_f \mathbf{F}_{jrf} \quad \text{momentum,} \\ d_t \int_j \rho e = - \sum_r \sum_f \mathbf{F}_{jrf} \cdot \mathbf{u}_r \quad \text{energy,} \end{array} \right. \quad (10)$$

where $\int_j \cdot$ denotes the integral over the cell Ω_j moving at the fluid velocity \mathbf{u} .

In the following, we denote $m_j := \int_j \rho$, $\mathbf{u}_j := \int_j \rho \mathbf{u} / \int_j \rho$, $e_j := \int_j \rho e / \int_j \rho$, and $\varepsilon_j := \int_j \rho \varepsilon / \int_j \rho$.

This system of equation is closed by the kinematic evolution of the node positions $d_t \mathbf{x}_r = \mathbf{u}_r$. An acoustic Riemann solver is employed to compute the fluxes \mathbf{F}_{jrf} and $\mathbf{F}_{jrf} \cdot \mathbf{u}_r$. The way this Riemann solver is expressed makes the difference between the semi-discrete schemes, but can be also put in the same formalism

$$\mathbf{F}_{jrf} - \mathbf{F}_j^{rf} + \rho_j c_j A_{jrf} (\mathbf{u}_r - \mathbf{u}_j) = \mathbf{0}, \quad (11)$$

where

$$\mathbf{F}_j^{rf} = \mathbf{N}_{jrf} p_j \quad (12)$$

is a reconstructed pressure force at the location considered, and A_{jrf} is a rank 1 symmetric non-negative matrix for Glace and Eucclhyd and a diagonal matrix for CCH¹. These matrices write

$$\left\{ \begin{array}{l} A_{jrf} = \frac{1}{\#(\mathcal{F}_{jr})} \frac{\mathbf{C}_{jr} \otimes \mathbf{C}_{jr}}{|\mathbf{C}_{jr}|} \quad \text{Glace,} \\ A_{jrf} = \mathbf{N}_{jrf} \otimes \mathbf{n}_{jrf} \quad \text{Eucclhyd,} \\ A_{jrf} = N_{jrf} |\mathbf{n}_{jrf} \cdot \mathbf{a}_j| Id \quad \text{CCH.} \end{array} \right. \quad (13)$$

¹in some case, a quadratic-like term proportional to $|\mathbf{u}_j - \mathbf{u}_r|$ is added to c_j in the above expression (11). We neglect this term in the analysis.

where Id stands for the identity $d \times d$ tensor (d being the dimension of the problem) and \mathbf{a}_j is the unit vector direction of the local acceleration. Whatever the scheme is, the matrix A_{jrf} is a purely geometric entity and scales as $\mathcal{O}(h_j)^{d-1}$ with respect to the cell radius h_j .

Summing equation (11) over all faces of all cells containing vertex r , and enforcing the momentum conservation, we get

$$A_r \mathbf{u}_r = \sum_j \sum_f \rho_j c_j A_{jrf} \mathbf{u}_j + \sum_j \mathbf{F}_j^{rf}, \quad (14)$$

where we define $A_r = \sum_j \sum_f \rho_j c_j A_{jrf}$. The matrix A_r can be proven to be invertible (refer to [9, 36]).

3. Analysis of the colocated schemes at low Mach number

We consider only the first-order version of the scheme, in the analysis.

3.1. Adimensional semi-discrete scheme

We perform the same rescaling to the semi-discrete scheme (10) than for the continuous system (5). The volume integral scales as L^d , and the geometrical vectors \mathbf{N}_{jrf} as L^{d-1} . Finally, since p_{jrf} has the dimension of a pressure, and \mathbf{u}_r has the dimension of a velocity, we obtain the following adimensional semi-discrete scheme:

$$\left\{ \begin{array}{l} d_{\bar{t}} \int_j 1 = \sum_r \bar{\mathbf{C}}_{jr} \cdot \bar{\mathbf{u}}_r \quad \text{volume,} \\ d_{\bar{t}} \int_j \bar{\rho} \bar{\mathbf{u}} = -\frac{1}{M^2} \sum_r \sum_f \bar{\mathbf{F}}_{jrf} \quad \text{momentum,} \\ d_{\bar{t}} \int_j \bar{\rho} \bar{e} = -\sum_r \sum_f \bar{\mathbf{F}}_{jrf} \cdot \bar{\mathbf{u}}_r \quad \text{energy.} \end{array} \right. \quad (15)$$

Same rescaling can be made for the acoustic Godunov solver. For equation (11):

$$\bar{\mathbf{F}}_{jrf} - \bar{\mathbf{F}}_j^{rf} + M \bar{\rho}_j \bar{c}_j \bar{A}_{jrf} (\bar{\mathbf{u}}_r - \bar{\mathbf{u}}_j) = \mathbf{0}, \quad (16)$$

and for equation (14):

$$\bar{A}_r \bar{\mathbf{u}}_r = \sum_j \sum_f \bar{\rho}_j \bar{c}_j \bar{A}_{jrf} \bar{\mathbf{u}}_j + \frac{1}{M} \sum_j \bar{\mathbf{F}}_j^{rf}. \quad (17)$$

3.2. Consistence of the spatial operators

We now prove that the semi-discrete scheme (15) with the nodal solver (16) and (17) is consistent with the continuous system (5) with an error proportional to $\frac{\bar{h}}{M}$, where $\bar{h} = \max_j(\bar{h}_j)$. To achieve that, we need the three following propositions.

Proposition 3.1. *Assume that $0 < \alpha_1 \leq \bar{\rho}_j \bar{c}_j \leq \alpha_2$ for all j , then*

$$\begin{aligned} \forall e \in \mathcal{J}_r, \quad \forall g \in \mathcal{F}_{er}, \\ |\bar{\mathbf{N}}_{erg} \cdot (\bar{\mathbf{u}}_r - \bar{\mathbf{u}}_e)| \leq \beta_0 \left(\max_{j,k \in \mathcal{J}_r} |\bar{\mathbf{u}}_j - \bar{\mathbf{u}}_k| + \frac{1}{M} \max_{j,k \in \mathcal{J}_r} |\bar{p}_j - \bar{p}_k| \right) \max_{j \in \mathcal{J}_r, f \in \mathcal{F}_{jr}} |\bar{\mathbf{N}}_{jrf}|, \end{aligned} \quad (18)$$

where β_0 does not depend on \bar{h} and M .

Proof. The proof mimicks the proof of proposition (10) in [20].

We have the identity $\bar{A}_r \bar{\mathbf{u}}_e = \sum_j \sum_f \bar{\mathbf{N}}_{jrf} \bar{\rho}_j \bar{c}_j \bar{\mathbf{u}}_e \cdot \mathbf{n}_{jrf}$. Using $\sum_j \sum_f \bar{\mathbf{N}}_{jrf} \bar{\mathbf{u}}_e = \mathbf{0}$, we recast the nodal solver (16) into

$$\bar{A}_r \mathbf{y}_r = \sum_j \sum_f \bar{\mathbf{N}}_{jrf} y_j, \quad (19)$$

where $\mathbf{y}_r = \bar{\mathbf{u}}_r - \bar{\mathbf{u}}_e$, and $y_j = (\bar{p}_j - \bar{p}_e) + \frac{\bar{\rho}_j \bar{c}_j}{M} (\bar{\mathbf{u}}_j - \bar{\mathbf{u}}_e) \cdot \mathbf{n}_{jrf}$. Multiplying equation (19) by \mathbf{y}_r , we obtain: $\mathbf{y}_r \bar{A}_r \mathbf{y}_r = \sum_j \sum_f y_j \bar{\mathbf{N}}_{jrf} \cdot \mathbf{y}_r$. Moreover, $\mathbf{y}_r \bar{A}_r \mathbf{y}_r = \sum_j \sum_f \frac{\bar{\rho}_j \bar{c}_j}{|\bar{\mathbf{N}}_{jrf}|} (\bar{\mathbf{N}}_{jrf} \cdot \mathbf{y}_r)^2$. Using the hypothesis of the proposition, it yields:

$$\sum_j \sum_f (\bar{\mathbf{N}}_{jrf} \cdot \mathbf{y}_r)^2 \leq \frac{\max_{j \in \mathcal{J}_r, f \in \mathcal{F}_{jr}} |\bar{\mathbf{N}}_{jrf}|}{\alpha_1} \sum_j \sum_f |y_j| |\bar{\mathbf{N}}_{jrf} \cdot \mathbf{y}_r|.$$

From the Cauchy-Schwarz inequality we infer:

$$\sum_j \sum_f |y_j| |\bar{\mathbf{N}}_{jrf} \cdot \mathbf{y}_r| \leq \sqrt{\sum_j \sum_f (\bar{\mathbf{N}}_{jrf} \cdot \mathbf{y}_r)^2} \sqrt{\sum_j \sum_f y_j^2},$$

and

$$\sum_j \sum_f |\bar{\mathbf{N}}_{jrf} \cdot \mathbf{y}_r| \leq \sqrt{\sum_j \sum_f (\bar{\mathbf{N}}_{jrf} \cdot \mathbf{y}_r)^2}.$$

Together with the previous inequalities, we obtain:

$$\sum_j \sum_f |\bar{\mathbf{N}}_{jrf} \cdot \mathbf{y}_r| \leq \frac{\max_{j \in \mathcal{J}_r, f \in \mathcal{F}_{jr}} |\bar{\mathbf{N}}_{jrf}|}{\alpha_1} \sqrt{\sum_j \sum_f y_j^2},$$

which ends the proof using the definition of y_j , since $\bar{\rho}_j$ and \bar{c}_j do not depend on M and \bar{h} . \square

Proposition 3.2. *Under the same condition than for proposition (3.1) we have,*

$$\begin{aligned} \forall e \in \mathcal{J}_r, \quad \forall g \in \mathcal{F}_{jr}, \\ |\bar{\mathbf{F}}_{erg} - \bar{\mathbf{F}}_e| \leq \beta_1 (M \max_{j,k \in \mathcal{J}_r} |\bar{\mathbf{u}}_j - \bar{\mathbf{u}}_k| + \max_{j,k \in \mathcal{J}_r} |\bar{p}_j - \bar{p}_k|) \max_{j \in \mathcal{J}_r, f \in \mathcal{F}_{jr}} |\bar{\mathbf{N}}_{jrf}|. \end{aligned} \quad (20)$$

where β_1 does not depend on \bar{h}_j and M .

Proof. Equation (16) gives $\bar{\mathbf{F}}_{jrf} - \bar{\mathbf{F}}_j^{rf} = M \bar{\rho}_j \bar{c}_j \bar{\mathbf{N}}_{jrf} (\bar{\mathbf{u}}_r - \bar{\mathbf{u}}_j) \cdot \bar{\mathbf{n}}_{jrf}$. Applying the proposition (3.1) implies the result. \square

Proposition 3.3. *Under the conditions of proposition (3.1) we have,*

$$\begin{aligned} \forall e \in \mathcal{J}_r, \quad \forall g \in \mathcal{F}_{jr}, \\ |\bar{\mathbf{N}}_{erg} \cdot \bar{\mathbf{u}}_r| \leq \beta_2 (\max_{j \in \mathcal{J}_r} |\bar{\mathbf{u}}_j| + \frac{1}{M} \max_{j \in \mathcal{J}_r} |\bar{p}_j|) \max_{j \in \mathcal{J}_r, f \in \mathcal{F}_{jr}} |\bar{\mathbf{N}}_{jrf}|, \end{aligned} \quad (21)$$

where β_2 does not depend on \bar{h}_j and M .

Proof. Equation (16) gives $\bar{\mathbf{N}}_{jrf} \bar{p}_{jrf} = \bar{\mathbf{N}}_{jrf} \bar{p}_j + M \bar{\rho}_j \bar{c}_j \bar{\mathbf{N}}_{jrf} (\bar{\mathbf{u}}_r - \bar{\mathbf{u}}_j) \cdot \bar{\mathbf{n}}_{jrf}$. Consequently, since $\bar{\mathbf{N}}_{jrf} \neq \mathbf{0}$, $\bar{\mathbf{N}}_{jrf} \cdot \bar{\mathbf{u}}_r = \bar{\mathbf{N}}_{jrf} \cdot \bar{\mathbf{u}}_j + \frac{1}{M \bar{\rho}_j \bar{c}_j} |\bar{\mathbf{N}}_{jrf}| (\bar{p}_{jrf} - \bar{p}_j)$.

Applying the proposition (3.2) gives the result.

Note that summing the previous equation on the faces sharing the cell j and the node r gives a similar estimate on $|\bar{\mathbf{C}}_{er} \cdot \bar{\mathbf{u}}_r|$. \square

In the following we use the convention that $\bar{\varphi}(\bar{\mathbf{x}}) = \sum_j \varphi_j 1_{\bar{\mathbf{x}} \in \bar{\Omega}_j}$, and $\bar{\mathbf{x}} \rightarrow 1_{\bar{\mathbf{x}}}$ is the indicator of characteristic function of cell $\bar{\Omega}_j$.

Defining $B(\bar{\mathbf{x}}) = \sum_j \left[\sum_r \sum_f \bar{\mathbf{F}}_{jrf} \right] \frac{1_{\bar{\mathbf{x}} \in \bar{\Omega}_j}}{|\bar{\Omega}_j|}$, we can now prove the weak consistency of the gradient operator.

Proposition 3.4. *Assume that $0 < \alpha_1 \leq \bar{\rho}_j \bar{c}_j \leq \alpha_2$ for all j , that the mesh is regular in the sense $\alpha_3 \bar{h}^d \leq |\bar{\Omega}_j|$ and $\bar{h}_j \leq \alpha_4 \bar{h}$ for all cells, with uniform constants $\alpha_1, \alpha_2, \alpha_3, \alpha_4 > 0$. Assume moreover that \bar{p}_j and $\bar{\mathbf{u}}_j$ are bounded in L^∞ and are bounded in the BV sense*

$$\sum_j \sum_{k \in \mathcal{J}_j} \bar{h}^{d-1} |\bar{\mathbf{u}}_j - \bar{\mathbf{u}}_k| \leq \alpha_5 \quad \text{and} \quad \sum_j \sum_{k \in \mathcal{J}_j} \bar{h}^{d-1} |\bar{p}_j - \bar{p}_k| \leq \alpha_6, \quad (22)$$

Assume also that

$$\forall j, |\bar{p}_j - \bar{p}_k|_{k \in \mathcal{J}_j} = \mathcal{O}(M^2) \quad (23)$$

then $B - \nabla \bar{p} = \mathcal{O}(M\bar{h})$ in the weak sense.

Before proving the result, some comments are in order.

- The hypothesis (23) is classical for low-Mach analysis, it is related to the fact that in the low-Mach regime, $\nabla \bar{p} = \mathcal{O}(M^2)$, and consequently $|\bar{p}_j - \bar{p}_k|_{k \in \mathcal{J}_j} = \mathcal{O}(M^2)$ (refer to the analysis in section 2.1). It implies also that $|\bar{p} - \bar{p}_m| = \mathcal{O}(M^2)$, where $\bar{p}_m = \frac{1}{|\Omega|} \int_{\Omega} \bar{p}$ is the mean adimensional pressure on Ω .
- The proposition can be rewritten in the following form: for any smooth function $\bar{\mathbf{x}} \rightarrow \varphi(\bar{\mathbf{x}})$ with compact support in Ω , $\int_{\Omega} B\varphi + \int_{\Omega} \bar{p}\nabla\varphi = \mathcal{O}(M\bar{h})$.
- In the proof, we make use of three following estimates concerning the mean of a smooth function

$$\frac{1}{|\bar{\Omega}_j|} \int_{\bar{\Omega}_j} \varphi d\bar{\mathbf{x}} - \varphi(\bar{\mathbf{x}}_j) = \mathcal{O}(\bar{h}^2), \quad (24)$$

the number of cells in the mesh

$$\#\mathcal{J} = \mathcal{O}(\bar{h}^{-d}), \quad (25)$$

and the size of $\bar{\mathbf{N}}_{jrf}$

$$|\bar{\mathbf{N}}_{jrf}| = \mathcal{O}(\bar{h}^{d-1}). \quad (26)$$

- We also use the following identity demonstrated for instance in [20]:

$$\sum_r \sum_f \bar{\mathbf{N}}_{jrf} \otimes \bar{\mathbf{x}}_r = |\bar{\Omega}_j| Id, \quad (27)$$

Proof. First part of the proof is the proof of the theorem 12 in [20]. It is demonstrated that

$$\int_{\Omega} B\varphi + \int_{\Omega} \bar{p}\nabla\varphi = \mathcal{O}(\bar{h}).$$

Introducing the definition of B into this expression, we obtain

$$\sum_j \frac{1}{|\bar{\Omega}_j|} \int_{\bar{\Omega}_j} \varphi d\bar{\mathbf{x}} \sum_r \sum_f \bar{\mathbf{F}}_{jrf} + \int_{\Omega} \bar{p}\nabla\varphi = R_r, \quad (28)$$

with $R_r = \mathcal{O}(\bar{h})$.

Second part consists in proving that

$$\sum_j \frac{1}{|\bar{\Omega}_j|} \int_{\Omega_j} \varphi d\bar{\mathbf{x}} \sum_r \sum_f \bar{\mathbf{F}}_{jrf} = \mathcal{O}(M) \text{ and } \int_{\Omega} \bar{p} \nabla \varphi = \mathcal{O}(M^2).$$

Using $\sum_r \sum_f \bar{\mathbf{F}}_j^{rf} = \mathbf{0}$, we infer

$$\sum_j \frac{1}{|\bar{\Omega}_j|} \int_{\Omega_j} \varphi d\bar{\mathbf{x}} \sum_r \sum_f \bar{\mathbf{F}}_{jrf} = \sum_j \frac{1}{|\bar{\Omega}_j|} \int_{\Omega_j} \varphi d\bar{\mathbf{x}} \sum_r \sum_f \left(\bar{\mathbf{F}}_{jrf} - \bar{\mathbf{F}}_j^{rf} \right).$$

Since φ is $\mathcal{O}(1)$ with respect to M , the proposition 3.2 and the Cauchy-Schwarz inequality give us

$$\begin{aligned} \left| \sum_j \frac{1}{|\bar{\Omega}_j|} \int_{\Omega_j} \varphi d\bar{\mathbf{x}} \sum_r \sum_f \left(\bar{\mathbf{F}}_{jrf} - \bar{\mathbf{F}}_j^{rf} \right) \right| &\leq \alpha \beta_1 (M \max_{j,k \in \mathcal{J}_r} |\bar{\mathbf{u}}_j - \bar{\mathbf{u}}_k| \\ &\quad + \max_{j,k \in \mathcal{J}_r} |\bar{p}_j - \bar{p}_k|) \max_{j \in \mathcal{J}_r, f \in \mathcal{F}_{j_r}} |\bar{\mathbf{N}}_{jrf}|, \end{aligned}$$

for some α which does not depend on M . Using the low-Mach hypothesis (23), we obtain

$$\left| \sum_j \frac{1}{|\bar{\Omega}_j|} \int_{\Omega_j} \varphi d\bar{\mathbf{x}} \sum_r \sum_f \left(\bar{\mathbf{F}}_{jrf} - \bar{\mathbf{F}}_j^{rf} \right) \right| = \mathcal{O}(M) + \mathcal{O}(M^2) = \mathcal{O}(M). \quad (29)$$

We study now the second term. Since φ has a compact support

$$\int_{\Omega} \bar{p} \nabla \varphi = \int_{\Omega} (\bar{p} - \bar{p}_m) \nabla \varphi,$$

where \bar{p}_m is the mean pressure over Ω .

Using the Cauchy-Schwarz inequality and the smoothness of φ , we infer

$$\begin{aligned} \left| \int_{\Omega} (\bar{p} - \bar{p}_m) \nabla \varphi \right| &\leq \sqrt{\int_{\Omega} |\bar{p} - \bar{p}_m|^2} \sqrt{\int_{\Omega} |\nabla \varphi|^2}, \\ &\leq \alpha \sqrt{\int_{\Omega} |\bar{p} - \bar{p}_m|^2}, \end{aligned}$$

for some α independant of M .

The low Mach hypothesis (23) gives us

$$\int_{\Omega} (\bar{p} - \bar{p}_m) \nabla \varphi = \mathcal{O}(M^2). \quad (30)$$

Plugging estimates (29) and (30) into (28), we infer that $R_r = \mathcal{O}(M)$, and since we also have that $R_r = \mathcal{O}(\bar{h})$, $R_r = \mathcal{O}(M\bar{h})$. □

It is worth noting that this proof already enlightens the issue of this solver for low-Mach flows. Indeed, the fact that the continuous gradient and the discrete one have not the same dependence with respect to the Mach number will produce spurious results in this regime.

Defining now $C(\bar{\mathbf{x}}) = \sum_j \left[\sum_r \bar{\mathbf{C}}_{jr} \cdot \bar{\mathbf{u}}_r \right] \frac{1_{\bar{\mathbf{x}} \in \bar{\Omega}_j}}{|\bar{\Omega}_j|}$, we can now prove the weak consistency of the divergence operator of the volume balance law.

Proposition 3.5. *Assume same hypothesis than proposition 3.4, then $C - \nabla \cdot \bar{\mathbf{u}} = \mathcal{O}(\bar{h})$ in the weak sense, independent from the Mach number.*

First part of the proof mimicks the proof of theorem (12) in [20], and demonstrates that $C - \nabla \cdot \bar{\mathbf{u}} = \mathcal{O}(\bar{h})$ in the weak sense, with respect to h . Second part of the proof demonstrates that $C - \nabla \cdot \bar{\mathbf{u}} = \mathcal{O}(1)$ in the weak sense with respect to M .

Proof. • We have

$$\int_{\Omega} C\varphi = \sum_j \frac{1}{|\bar{\Omega}_j|} \int_{\Omega_j} \varphi d\bar{\mathbf{x}} \sum_r \bar{\mathbf{C}}_{jr} \cdot \bar{\mathbf{u}}_r.$$

Introducing the $\varphi(\bar{\mathbf{x}}_j)$ into this formula gives:

$$\begin{aligned} \int_{\Omega} C\varphi &= \sum_j \varphi(\bar{\mathbf{x}}_j) \sum_r \bar{\mathbf{C}}_{jr} \cdot \bar{\mathbf{u}}_r + \sum_j \left(\frac{1}{|\bar{\Omega}_j|} \int_{\Omega_j} \varphi d\bar{\mathbf{x}} - \varphi(\bar{\mathbf{x}}_j) \right) \sum_r \bar{\mathbf{C}}_{jr} \cdot \bar{\mathbf{u}}_r, \\ &= \sum_j \varphi(\bar{\mathbf{x}}_j) \sum_r \bar{\mathbf{C}}_{jr} \cdot \bar{\mathbf{u}}_r + \sum_j \left(\frac{1}{|\bar{\Omega}_j|} \int_{\Omega_j} \varphi d\bar{\mathbf{x}} - \varphi(\bar{\mathbf{x}}_j) \right) \sum_r \bar{\mathbf{C}}_{jr} \cdot (\bar{\mathbf{u}}_r - \bar{\mathbf{u}}_j), \end{aligned}$$

since $\sum_r \bar{\mathbf{C}}_{jr} = \mathbf{0}$.

Using proposition 3.2, estimates (24), (25) and (26), and last inequality of (9), we infer

$$\sum_j \left(\frac{1}{|\bar{\Omega}_j|} \int_{\Omega_j} \varphi d\bar{\mathbf{x}} - \varphi(\bar{\mathbf{x}}_j) \right) \sum_r (\bar{\mathbf{C}}_{jr} \cdot (\bar{\mathbf{u}}_r - \bar{\mathbf{u}}_j)) = \mathcal{O}(\bar{h}^2) \mathcal{O}(\bar{h}^{-d}) \mathcal{O}(\bar{h}^{d-1}) = \mathcal{O}(\bar{h}).$$

Moreover, since $\sum_j \bar{\mathbf{C}}_{jr} \cdot \bar{\mathbf{u}}_r = \mathbf{0}$,

$$\begin{aligned} \sum_j \varphi(\bar{\mathbf{x}}_j) \sum_r \bar{\mathbf{C}}_{jr} \cdot \bar{\mathbf{u}}_r &= \sum_j \sum_r \bar{\mathbf{C}}_{jr} \cdot \bar{\mathbf{u}}_r (\varphi(\bar{\mathbf{x}}_j) - \varphi(\bar{\mathbf{x}}_r)) \\ &= \sum_j \sum_r \bar{\mathbf{C}}_{jr} \cdot \bar{\mathbf{u}}_j (\varphi(\bar{\mathbf{x}}_j) - \varphi(\bar{\mathbf{x}}_r)) + \sum_j \sum_r (\bar{\mathbf{C}}_{jr} \cdot (\bar{\mathbf{u}}_r - \bar{\mathbf{u}}_j)) (\varphi(\bar{\mathbf{x}}_j) - \varphi(\bar{\mathbf{x}}_r)) \end{aligned}$$

Since φ is smooth, $\varphi(\bar{\mathbf{x}}_j) - \varphi(\bar{\mathbf{x}}_r) = \mathcal{O}(\bar{h})$, and

$$\sum_j \sum_r (\bar{\mathbf{C}}_{jr} \cdot (\bar{\mathbf{u}}_r - \bar{\mathbf{u}}_j)) (\varphi(\bar{\mathbf{x}}_j) - \varphi(\bar{\mathbf{x}}_r)) = \mathcal{O}(\bar{h}^{1-d}) \mathcal{O}(\bar{h}^{d-1}) \mathcal{O}(\bar{h}) = \mathcal{O}(\bar{h}),$$

using the BV hypothesis (22).

The smoothness of φ implies $\varphi(\bar{\mathbf{x}}_r) = \varphi(\bar{\mathbf{x}}_j) + \nabla\varphi(\bar{\mathbf{x}}_j) \cdot (\bar{\mathbf{x}}_r - \bar{\mathbf{x}}_j) + \mathcal{O}(\bar{h}^2)$, and then using similar arguments as before

$$\begin{aligned} \sum_j \sum_r \bar{\mathbf{C}}_{jr} \cdot \bar{\mathbf{u}}_j (\varphi(\bar{\mathbf{x}}_j) - \varphi(\bar{\mathbf{x}}_r)) &= \sum_j \sum_r \bar{\mathbf{C}}_{jr} \cdot \bar{\mathbf{u}}_j \nabla\varphi(\bar{\mathbf{x}}_j) \cdot (\bar{\mathbf{x}}_r - \bar{\mathbf{x}}_j) + \mathcal{O}(\bar{h}) \\ &= \sum_j \bar{\mathbf{u}}_j \sum_r \bar{\mathbf{C}}_{jr} \otimes \bar{\mathbf{x}}_r \nabla\varphi(\bar{\mathbf{x}}_j) + \mathcal{O}(\bar{h}) \end{aligned}$$

Using relation (27), we infer:

$$\begin{aligned} \sum_j \bar{\mathbf{u}}_j \sum_r \bar{\mathbf{C}}_{jr} \otimes \bar{\mathbf{x}}_r \cdot \nabla\varphi(\bar{\mathbf{x}}_j) &= \sum_j |\bar{\Omega}_j| \bar{\mathbf{u}}_j \cdot \nabla\varphi(\bar{\mathbf{x}}_j) \\ &= - \int_{\Omega} \bar{\mathbf{u}} \cdot \nabla\varphi(\bar{\mathbf{x}}) + \mathcal{O}(\bar{h}) \end{aligned}$$

Putting all these pieces together, it proves the first part of the claim, that is $R_e = \mathcal{O}(\bar{h})$.

- Now, we prove that $\int_{\Omega} C\varphi$ and $\int_{\Omega} \bar{\mathbf{u}} \cdot \nabla\varphi(\bar{\mathbf{x}})$ are $\mathcal{O}(1)$ with respect to M .

Since $\bar{\mathbf{u}}$ and $\nabla\varphi$ are $\mathcal{O}(1)$, we conclude easily that $\int_{\Omega} \bar{\mathbf{u}} \cdot \nabla\varphi(\bar{\mathbf{x}}) = \mathcal{O}(1)$.

Moreover, we have

$$\begin{aligned} \int_{\Omega} C\varphi &= \sum_j \frac{1}{|\bar{\Omega}_j|} \int_{\bar{\Omega}_j} \varphi d\bar{\mathbf{x}} \sum_r \bar{\mathbf{C}}_{jr} \cdot \bar{\mathbf{u}}_r, \\ &= \sum_j \frac{1}{|\bar{\Omega}_j|} \int_{\bar{\Omega}_j} \varphi d\bar{\mathbf{x}} \sum_r \bar{\mathbf{C}}_{jr} \cdot (\bar{\mathbf{u}}_r - \bar{\mathbf{u}}_j). \end{aligned}$$

Using the fact that $\varphi(\bar{\mathbf{x}}) = \mathcal{O}(1)$ with respect to M , the proposition (3.1) and the low Mach assumption (23), we infer that $\int_{\Omega} C\varphi = \mathcal{O}(1)$ with respect to M . It proves the claims. \square

Defining now $D(\bar{\mathbf{x}}) = \sum_j \left[\sum_r \sum_f \bar{\mathbf{F}}_{jrf} \cdot \bar{\mathbf{u}}_r \right] \frac{1_{\bar{\mathbf{x}} \in \bar{\Omega}_j}}{|\bar{\Omega}_j|}$, we can now prove the weak consistency of the energy flux.

Proposition 3.6. *Assume same hypothesis than proposition 3.4, then $D - \nabla \cdot \bar{p}\bar{\mathbf{u}} = \mathcal{O}(\bar{h})$ in the weak sense, independant from the Mach number.*

Proof. The first part of the proof can be found in [20] and is not reproduced here. It concludes that $D - \nabla \cdot \bar{p}\bar{\mathbf{u}} = \mathcal{O}(\bar{h})$ in the weak sense with respect to the mesh size. It means, that

$$\sum_j \frac{1}{|\bar{\Omega}_j|} \int_{\Omega_j} \varphi d\bar{\mathbf{x}} \sum_r \sum_f \bar{\mathbf{F}}_{jrf} \cdot \bar{\mathbf{u}}_r + \int_{\Omega} \bar{p}\bar{\mathbf{u}} \nabla \varphi = R_e,$$

with $R_e = \mathcal{O}(\bar{h})$.

Now we prove that R_e is $\mathcal{O}(1)$ with respect to the Mach number.

- Since $\bar{\mathbf{u}}$, \bar{p} and $\nabla \varphi$ are $\mathcal{O}(1)$, $\int_{\Omega} \bar{p}\bar{\mathbf{u}} \nabla \varphi = \mathcal{O}(1)$.

- Now concerning the first part of the left-hand-side:

$$\begin{aligned} & \sum_j \frac{1}{|\bar{\Omega}_j|} \int_{\Omega_j} \varphi d\bar{\mathbf{x}} \sum_r \sum_f \bar{\mathbf{F}}_{jrf} \cdot \bar{\mathbf{u}}_r = \\ & \sum_j \frac{1}{|\bar{\Omega}_j|} \int_{\Omega_j} \varphi d\bar{\mathbf{x}} \sum_r \sum_f \left(\bar{\mathbf{F}}_{jrf} - \bar{\mathbf{F}}_j^{rf} \right) \cdot (\bar{\mathbf{u}}_r - \bar{\mathbf{u}}_j) + \bar{\mathbf{F}}_j^{rf} \cdot \bar{\mathbf{u}}_r, \end{aligned}$$

since $\sum_r \sum_f \bar{\mathbf{F}}_{jrf} \cdot \bar{\mathbf{u}}_j = \mathbf{0}$, and $\sum_r \sum_f \bar{\mathbf{F}}_j^{rf} \bar{\mathbf{u}}_j = \mathbf{0}$. It is easy to check using propositions 3.1, 3.2 and the hypothesis of the current proposition, that $\sum_r \sum_f \left(\bar{\mathbf{F}}_{jrf} - \bar{\mathbf{F}}_j^{rf} \right) \cdot (\bar{\mathbf{u}}_r - \bar{\mathbf{u}}_j) = \mathcal{O}(M)$. Using proposition 3.3, we find that $\sum_r \sum_f \bar{\mathbf{F}}_j^{rf} \cdot \bar{\mathbf{u}}_r = \mathcal{O}(1)$, with respect to the Mach number. Consequently, we have proven that $\sum_j \frac{1}{|\bar{\Omega}_j|} \int_{\Omega_j} \varphi d\bar{\mathbf{x}} \sum_r \sum_f \bar{\mathbf{F}}_{jrf} \bar{\mathbf{u}}_r = \mathcal{O}(1)$ with respect to the Mach number. □

Plugging these estimates into the semi-discrete solver (15), we finally obtain the equivalent equations:

$$\begin{cases} d_{\bar{t}} \int_j 1 &= \int_j \nabla \cdot \bar{\mathbf{u}} + \mathcal{O}(\bar{h}) & \text{volume,} \\ d_{\bar{t}} \int_j \bar{p}\bar{\mathbf{u}} &= - \int_j \frac{1}{M^2} \nabla \bar{p} + \mathcal{O}\left(\frac{\bar{h}}{M}\right) & \text{momentum,} \\ d_{\bar{t}} \int_j \bar{p}\bar{e} &= - \int_j \nabla \cdot (\bar{p}\bar{\mathbf{u}}) + \mathcal{O}(\bar{h}) & \text{energy.} \end{cases} \quad (31)$$

This analysis explains the bad behavior of this scheme in the low-Mach regime, since the momentum equation suffer of a $\mathcal{O}(\frac{1}{M})$ error.

Similar analysis on the entropy balance shows that

$$T_j d_{\bar{t}} \int_j \bar{\rho} \bar{\eta} = \mathcal{O}(\bar{M}) \quad (32)$$

what is one order of magnitude higher with respect to M than what is expected from the continuous analysis.

4. Low-Mach correction of the colocated schemes

We now propose a low-Mach correction for colocated Godunov schemes, and prove the consistency of the resulting semi-discrete scheme.

4.1. Modified scheme

Following the ideas developed for instance in [18], the pressure gradient should be centered at low Mach number, cancelling the dissipative velocity related term in the flux. This is why we propose the following modification of the fluxes:

$$\mathbf{G}_{jrf} = \lambda_r \mathbf{F}_{jrf} + (1 - \lambda_r) \mathbf{H}_{jrf}, \quad (33)$$

with $\lambda_r \in [0, 1] \subset \mathbb{R}$, and

$$\mathbf{H}_{jrf} = \mathbf{N}_{jrf} p_r, \quad (34)$$

where p_r is a consistent evaluation of the pressure at the node depending only on the p_j 's. Choices of λ_r and p_r are discussed in section 5.

The system (10) is recasted in:

$$\left\{ \begin{array}{ll} d_t \int_j 1 = \sum_r \mathbf{C}_{jr} \cdot \mathbf{u}_r & \text{volume,} \\ d_t \int_j \rho \mathbf{u} = - \sum_r \sum_f \mathbf{G}_{jrf} & \text{momentum,} \\ d_t \int_j \rho e = - \sum_r \sum_f \mathbf{G}_{jrf} \cdot \mathbf{u}_r & \text{energy,} \end{array} \right. \quad (35)$$

Computation of \mathbf{F}_{jrf} and \mathbf{u}_r does not change with respect to the classical scheme and are always given by equations (11) and (14). We check easily that the scheme remains conservative since $\sum_r \sum_j \sum_f \mathbf{H}_{jrf} = \sum_r p_r \sum_j \sum_f \mathbf{N}_{jrf} =$

$\mathbf{0}$.

4.2. Adimensional scheme

The adimensional counterpart of (35) is very similar to (15)

$$\left\{ \begin{array}{l} d_{\bar{t}} \int_j 1 = \sum_r \bar{\mathbf{C}}_{jr} \cdot \bar{\mathbf{u}}_r \quad \text{volume,} \\ d_{\bar{t}} \int_j \bar{\rho} \bar{\mathbf{u}} = -\frac{1}{M^2} \sum_r \sum_f \bar{\mathbf{G}}_{jrf} \quad \text{momentum,} \\ d_{\bar{t}} \int_j \bar{\rho} \bar{e} = -\sum_r \sum_f \bar{\mathbf{G}}_{jrf} \cdot \bar{\mathbf{u}}_r \quad \text{energy.} \end{array} \right. \quad (36)$$

Computation of $\bar{\mathbf{F}}_{jrf}$ and $\bar{\mathbf{u}}_r$ does not change with respect to the classical scheme and are always given by equations (16) and (17).

4.3. Uniform consistence of the spatial operators

We now demonstrate that the scheme defined by equations (35, 11, 14, 33) is consistent with the continuous system (1) uniformly with respect to the Mach number M .

Defining $B(\bar{\mathbf{x}}) = \sum_j \left[\sum_r \sum_f \bar{\mathbf{G}}_{jrf} \right] \frac{1_{\bar{\mathbf{x}} \in \bar{\Omega}_j}}{|\bar{\Omega}_j|}$, we now prove the weak consistency of the gradient operator.

Proposition 4.1. *Assume that $0 < \alpha_1 \leq \bar{\rho}_j \bar{c}_j \leq \alpha_2$ for all j , that the mesh is regular in the sense $\alpha_3 \bar{h}^d \leq |\bar{\Omega}_j|$ and $\bar{h}_j \leq \alpha_4 \bar{h}$ for all cells, with uniform constants $\alpha_1, \alpha_2, \alpha_3, \alpha_4 > 0$. Assume moreover that \bar{p}_j and $\bar{\mathbf{u}}_j$ are bounded in L^∞ and are bounded in the BV sense*

$$\sum_j \sum_{k \in \mathcal{J}_j} \bar{h}^{d-1} |\bar{\mathbf{u}}_j - \bar{\mathbf{u}}_k| \leq \alpha_5 \quad \text{and} \quad \sum_j \sum_{k \in \mathcal{J}_j} \bar{h}^{d-1} |\bar{p}_j - \bar{p}_k| \leq \alpha_6. \quad (37)$$

Assume also that

$$\forall j, |\bar{p}_j - \bar{p}_k|_{k \in \mathcal{J}_j} = \mathcal{O}(M^2) \quad (38)$$

and that

$$\forall j, k, r, \bar{\mathbf{G}}_{jrk} = \alpha M \bar{\mathbf{F}}_{jrk} + (1 - \alpha M) \bar{\mathbf{H}}_{jrk} \quad (39)$$

with $\alpha \in [0, 1]$, and $\alpha M \leq 1$, then $B - \nabla \bar{p} = \mathcal{O}(M^2 h)$ in the weak sense.

Note that the condition (39) enforces λ_r to be proportional to M . In this case, this scheme can be viewed as a multi-D generalization of the 1D scheme proposed in [10]. Since $\bar{\mathbf{G}}_{jrf}$ is a convex-combinaison of $\bar{\mathbf{F}}_{jrf}$ and $\bar{\mathbf{H}}_{jrf}$, the proof consists in three steps.

1. First step demonstrates that

$$\sum_j \frac{1}{|\bar{\Omega}_j|} \int_{\bar{\Omega}_j} \varphi d\bar{\mathbf{x}} \sum_r \sum_f \bar{\mathbf{F}}_{jrf} + \int_{\Omega} \bar{p} \nabla \varphi = \mathcal{O}(\bar{h}). \quad (40)$$

2. Second step is to prove that

$$\sum_j \frac{1}{|\bar{\Omega}_j|} \int_{\Omega_j} \varphi d\bar{\mathbf{x}} \sum_r \sum_f \bar{\mathbf{H}}_{jrf} + \int_{\Omega} \bar{p} \nabla \varphi = \mathcal{O}(\bar{h}). \quad (41)$$

3. Third step consists in showing that

$$\sum_j \frac{1}{|\bar{\Omega}_j|} \int_{\Omega_j} \varphi d\bar{\mathbf{x}} \sum_r \sum_f \bar{\mathbf{G}}_{jrf} = \mathcal{O}(M^2) \text{ and } \int_{\Omega} \bar{p} \nabla \varphi = \mathcal{O}(M^2). \quad (42)$$

Proof. 1. First step of the proof is the proof of the theorem 12 in [20].

2. Second step of the proof is very similar to the proof of proposition 3.5.

We use the following (obvious) estimates:

$$|\bar{p}_j - \bar{p}_r| \leq \max_{k \in \mathcal{J}_r} |\bar{p}_j - \bar{p}_k| \text{ and } \bar{p}_r \leq \max_{k \in \mathcal{J}_r} \bar{p}_k \quad (43)$$

The sketch of the remaining of the proof, very similar to the proof of proposition 3.4 is as follows:

$$\begin{aligned} \sum_j \frac{1}{|\bar{\Omega}_j|} \int_{\Omega_j} \varphi d\bar{\mathbf{x}} \sum_r \sum_f \bar{\mathbf{H}}_{jrf} &= \sum_j \varphi(\bar{\mathbf{x}}_j) \sum_r \sum_f \bar{\mathbf{H}}_{jrf} + \mathcal{O}(\bar{h}) \\ &= \sum_j \sum_r \sum_f \bar{\mathbf{H}}_{jrf} (\varphi(\bar{\mathbf{x}}_j) - \varphi(\bar{\mathbf{x}}_r)) + \mathcal{O}(\bar{h}) \\ &= \sum_j \sum_r \sum_f \bar{\mathbf{H}}_{jrf} \nabla \varphi(\bar{\mathbf{x}}_j) \cdot (\bar{\mathbf{x}}_j - \bar{\mathbf{x}}_r) + \mathcal{O}(\bar{h}) \\ &= \sum_j \sum_r \sum_f \bar{\mathbf{N}}_{jrf} \bar{p}_j \nabla \varphi(\bar{\mathbf{x}}_j) \cdot (\bar{\mathbf{x}}_j - \bar{\mathbf{x}}_r) + \mathcal{O}(\bar{h}) \\ &= - \sum_j \bar{p}_j \nabla \varphi(\bar{\mathbf{x}}_j) |\bar{\Omega}_j| + \mathcal{O}(\bar{h}) \\ &= - \int_{\Omega} \bar{p} \nabla \varphi(\bar{\mathbf{x}}) + \mathcal{O}(\bar{h}) \end{aligned}$$

3. As for the propositions 3.4, 3.5, and 3.6, the last step of the proof consists in showing that $\sum_j \frac{1}{|\bar{\Omega}_j|} \int_{\Omega_j} \varphi d\bar{\mathbf{x}} \sum_r \sum_f \bar{\mathbf{G}}_{jrf} = \mathcal{O}(M^2)$ and $-\int_{\Omega} \bar{p} \nabla \varphi(\bar{\mathbf{x}}) = \mathcal{O}(M^2)$.

The latter has been already proven in proposition 3.4. Concerning the former, we have shown in proposition 3.4 that $\sum_j \frac{1}{|\bar{\Omega}_j|} \int_{\Omega_j} \varphi d\bar{\mathbf{x}} \sum_r \sum_f \bar{\mathbf{F}}_{jrf} =$

$\mathcal{O}(M)$ and consequently

$$\alpha M \sum_j \frac{1}{|\bar{\Omega}_j|} \int_{\Omega_j} \varphi d\bar{\mathbf{x}} \sum_r \sum_f \bar{\mathbf{F}}_{jrf} = \mathcal{O}(M^2).$$

It remains to prove that $\sum_j \frac{1}{|\Omega_j|} \int_{\Omega_j} \varphi d\bar{\mathbf{x}} \sum_r \sum_f \bar{\mathbf{H}}_{jrf} = \mathcal{O}(M^2)$, which means that $\sum_r \sum_f \bar{\mathbf{H}}_{jrf} = \mathcal{O}(M^2)$. Using $\sum_r \sum_f \bar{\mathbf{N}}_{jrf} p_j = \mathbf{0}$, we infer

$$\sum_r \sum_f \bar{\mathbf{H}}_{jrf} = \sum_r \sum_f \bar{\mathbf{N}}_{jrf} (p_r - p_j).$$

The low-Mach hypothesis (38) and the Cauchy-Schwarz inequality allow to conclude. \square

With this modification, we have removed the issue observed with the classical scheme concerning the low-Mach regime.

Considering again $C(\bar{\mathbf{x}}) = \sum_j \left[\sum_r \bar{\mathbf{C}}_{jr} \cdot \bar{\mathbf{u}}_r \right] \frac{1_{\bar{\mathbf{x}} \in \bar{\Omega}_j}}{|\bar{\Omega}_j|}$, we can now prove the weak consistency of the divergence operator of the volume balance law.

Proposition 4.2. *Assume same hypothesis than proposition 4.1, then $C - \nabla \cdot \bar{\mathbf{u}} = \mathcal{O}(\bar{h})$ in the weak sense with respect to \bar{h} and M .*

Proof. This proof is exactly the same than those of proposition 3.5. \square

Defining now $D(\bar{\mathbf{x}}) = \sum_j \left[\sum_r \bar{\mathbf{G}}_{jrf} \bar{\mathbf{u}}_r \right] \frac{1_{\bar{\mathbf{x}} \in \bar{\Omega}_j}}{|\bar{\Omega}_j|}$, we can now prove the weak consistency of the energy flux.

Proposition 4.3. *Assume same hypothesis than proposition 4.1, then $D - \nabla \cdot \bar{p}\bar{\mathbf{u}} = \mathcal{O}(\bar{h})$ in the weak sense with respect to \bar{h} and M .*

Proof. The proof is very similar to the one of proposition 4.1. \square

Plugging these estimates into the semi-discrete system (36), we construct the equivalent equations:

$$\begin{cases} d_{\bar{t}} \int_j 1 &= \int_j \nabla \cdot \bar{\mathbf{u}} + \mathcal{O}(\bar{h}) & \text{volume,} \\ d_{\bar{t}} \int_j \bar{\rho}\bar{\mathbf{u}} &= - \int_j \frac{1}{M^2} \nabla \bar{p} + \mathcal{O}(\bar{h}) & \text{momentum,} \\ d_{\bar{t}} \int_j \bar{\rho}\bar{e} &= - \int_j \nabla \cdot (\bar{p}\bar{\mathbf{u}}) + \mathcal{O}(\bar{h}) & \text{energy.} \end{cases} \quad (44)$$

what shows the uniform consistency of the modified scheme with respect to M , that is an asymptotic preserving behaviour for the semi-discrete scheme.

5. Entropy condition and calculation of λ_r

In this section, we show that the definition of λ_r proposed in the previous section is compatible with the entropy condition.

We consider the semi-discrete entropy equation for the modified scheme. From the Gibbs relation, and assuming the spatial first-order accuracy of the scheme, we infer

$$T_j d_t \int_j \rho \eta = d_t \int_j \rho e - \mathbf{u}_j d_t \int_j \rho \mathbf{u} + p_j d_t \int_j 1. \quad (45)$$

Entropy condition implies $T_j d_t \int_j \rho \eta \geq 0$.

Proposition 5.1. *A sufficient condition to enforce the growth of the entropy for the semi-discrete scheme (35) is*

$$\lambda_r = \max_{j \in \mathcal{F}_r} \left(\frac{|p_j - p_r|}{|p_j - p_r| + |p_j - p_{jrf}|} \right). \quad (46)$$

Proof. Plugging the fluxes of the scheme (35) into equation (45), the entropy condition recasts:

$$- \sum_r \sum_f \mathbf{G}_{jrf} \cdot \mathbf{u}_r + \mathbf{u}_j \cdot \sum_r \sum_f \mathbf{G}_{jrf} + p_j \sum_r \sum_f \mathbf{N}_{jrf} \cdot \mathbf{u}_r \geq 0.$$

Since $\sum_r \sum_f \mathbf{N}_{jrf} \cdot \mathbf{u}_j = \mathbf{0}$, this equation is equivalent to

$$\sum_r \sum_f (\mathbf{N}_{jrf} p_j - \mathbf{G}_{jrf}) \cdot (\mathbf{u}_r - \mathbf{u}_j) \geq 0.$$

Using the definition of \mathbf{G}_{jrf} , this expression can be recasted into:

$$\sum_r \sum_f \lambda_r (\mathbf{N}_{jrf} p_j - \mathbf{F}_{jrf}) \cdot (\mathbf{u}_r - \mathbf{u}_j) \geq \sum_r (1 - \lambda_r) (\mathbf{N}_{jrf} p_j - \mathbf{H}_{jrf}) \cdot (\mathbf{u}_j - \mathbf{u}_r). \quad (47)$$

The good news is that the Left-Hand-Side of this inequality is positive thanks to the Riemann solver (11). Unfortunately, the sign of the Right-Hand-Side of the inequality is not determined. However, a sufficient condition for the inequality (47) to hold, is that

$$\forall r \in \mathcal{R}_j, \forall f \in \mathcal{F}_{jr}, \lambda_r (\mathbf{N}_{jrf} p_j - \mathbf{F}_{jrf}) \cdot (\mathbf{u}_r - \mathbf{u}_j) \geq (1 - \lambda_r) (\mathbf{N}_{jrf} p_j - \mathbf{H}_{jrf}) \cdot (\mathbf{u}_j - \mathbf{u}_r).$$

The problematic case corresponds to $\lambda_r (\mathbf{N}_{jrf} p_j - \mathbf{F}_{jrf}) \cdot (\mathbf{u}_r - \mathbf{u}_j) (1 - \lambda_r) (\mathbf{N}_{jrf} p_j - \mathbf{H}_{jrf}) \cdot (\mathbf{u}_j - \mathbf{u}_r) \leq 0$ (otherwise, both terms contribute to the increase of the entropy). Then, easy manipulations yield the following equivalent form

$$\forall r \in \mathcal{R}_j, \forall f \in \mathcal{F}_{jrf}, [\lambda_r(p_j - p_{jrf}) + (1 - \lambda_r)(p_j - p_r)] \mathbf{N}_{jrf} \cdot (\mathbf{u}_r - \mathbf{u}_j) \geq 0.$$

Thanks to the Riemann solver (11), we know that $(p_j - p_{jrf})$ and $\mathbf{N}_{jrf} \cdot (\mathbf{u}_r - \mathbf{u}_j)$ have the same sign. Consequently, a sufficient condition for inequality (47) to hold is

$$\forall r \in \mathcal{R}_j, \forall f \in \mathcal{F}_{jrf}, \lambda_r |p_j - p_{jrf}| \geq (1 - \lambda_r) |p_j - p_r|,$$

which gives

$$\forall r \in \mathcal{R}_j, \forall f \in \mathcal{F}_{jrf}, \lambda_r \geq \frac{|p_j - p_r|}{|p_j - p_r| + |p_j - p_{jrf}|}.$$

Since this inequality should hold for all cells, it ends the proof. \square

Weaker conditions can be obtain on λ_r considering the cases for which $p_j - p_r$ has the same sign than $p_j - p_{jrf}$ (no constraint induced).

We now demonstrate that the definition of λ_r fullfils the conditions of proposition 4.1, that is $\lambda_r = \mathcal{O}(M)$.

Proposition 5.2. *Assuming same hypothesis than for proposition 3.4, the coefficient λ_r defined by equation (46) is $\mathcal{O}(M)$.*

Proof. The definition of λ_r remains unchanged in adimensional form, and then estimate (23) and proposition 3.2 give the result. \square

These results prove that the hypothesis of proposition 3.4 are compatible with the entropy condition for the scheme (35).

Consequently, the new semi-discrete scheme defined by equations (35), (33), (46), (11) and (14) is

- conservative,
- endowed with a semi-dicrete entropy inequality,
- uniformly convergent with respect to the Mach number,
- Galilean invariant (since are the original scheme and the modification).

6. Implementation

The method has been implemented into the High Performance Computing framework [24], and use domain decomposition for parallel calculations. Since the CPU cost of the original scheme is mainly related to geometrical calculations (Volumes, \mathbf{C}_{jr} , MUSCL extension, . . .), the modification of the scheme induces a negligible additional CPU cost.

Considering the previous analysis, the only remaining degree of freedom of the method concerns the calculation of p_r in formula (34). The implementation of the entropy enforcing value of λ_r requires also explanations. In the following, we discuss the implementation choices we have made. We also adress the time-discretization issue and propose a formal second-order extension of the method.

6.1. Numerical parameters

Theoretically, any consistent formula to compute p_r fulfill the requirements for a low-Mach number version of the scheme. In this work, we simply use an average of the pressures in the cells surrounding each node, weighted by the cell volume. This procedure may be not optimal and more clever solutions can be considered, but we obtain satisfactory results with this basic approach.

In the following test problems, we also provide results with the formula

$$\begin{cases} \lambda_r = \max_{j \in \mathcal{J}_r} \left\{ \frac{|\mathbf{u}_j|}{c_j} \right\} & \text{if } \frac{|\mathbf{u}_j|}{c_j} \leq M_{max} \\ \lambda_r = 1 & \text{otherwise} \end{cases} \quad (48)$$

In the section 7, we take $M_{max} = 1$, but reasonably smaller values of M_{max} (> 0.5) have very few influence on the results. Note that the entropy stability criterion is no more fulfilled in this case for Mach numbers smaller than M_{max} , even if the scheme remains consistent for the entropy equation. Results using this formula for the calculation of λ_r are referred as **bmodified** (for basic modification) in the section 7.

We obviously provide results with the criterion (46). However this criterion requires a careful implementation for at least two reasons.

1. It does not tends to one in sonic or supersonic areas, while our goal is to recover the original Eucclhyd or Glace solvers in these areas. To deals with this problem, we enforce $\lambda_r \geq \min(1, \max_{j \in \mathcal{J}_r} \{M_j\})$. It gives the following formula for λ_r :

$$\lambda_r = \min \left(1, \max \left(\max_{j \in \mathcal{J}_r} \left(\frac{|p_j - p_r|}{|p_j - p_r| + |p_j - p_{jrf}|} \right), \max_{j \in \mathcal{J}_r} \{M_j\} \right) \right) \quad (49)$$

2. In quasi-steady areas, for which both $|p_j - p_r| \approx 0$ and $|p_j - p_{jrf}| \approx 0$, the criteria is not well defined and can lead to noisy values of λ_r . To cure this flaw, we take into account in the computation of λ_r only cells for which $|p_j - p_r| \geq (\Delta p)_{\min}$. The quality of the results are found quite sensitive to the choice of $(\Delta p)_{\min}$ in low-Mach regime while very few sensitive in supersonic regime. In the section 7, all results correspond to the choice $(\Delta p)_{\min} = 10^{-3}h_j$ (where h_j is the cell radius).
3. It is worth noting that we loose the Galilean invariance in introducing explicitly the Mach number into these formula. It can be recovered in using Galilean invariant evaluation of the Mach number as $M = |\mathbf{u} - \mathbf{u}_{\text{mean}}|/c$, where \mathbf{u}_{mean} is a local evaluation of the mean velocity.

Results obtained with this computation of λ_r will be referred as **emodified** (for entropic modified), while results obtained with the scheme without modification will be referred as **standard** in the section 7.

6.2. Time discretization

For the time integration, we use a forward Euler discretization and a second-order Runge-Kutta discretization for respectively the first-order and the second-order versions of the scheme.

With an implicit discrete in time scheme, all the properties established in the semi-discrete framework, including the entropy stability should remain valid. However, implicit schemes are hard to design in Lagrangian frame, and their efficiency is not demonstrated, in particular in the cases for which several Mach regimes coexist. Consequently, the correction we propose in this work is not fully asymptotic preserving, in the sense that the stability criteria of the scheme still depends on the Mach number (asymptotic preserving schemes for which the time-step does not depend on the Mach number are called «*all-regime*» [10, 11] or «*all-speed*» [16, 31, 32] in the litterature, and rely generally to a full- or a semi-implicitation). However, it is not a big issue, since our goal is to compute problems for which several Mach regimes coexist. In these cases, our experience is that the time-steps imposed by the stability criterion in the low-speed regions are of the same order of magnitude (and then not drastically more restrictive) than those computed in the high-speed ones. Moreover, using an implicit scheme in high Mach region lower the precision of the calculations and requires the resolution of a linear system.

In the numerical illustrations proposed hereafter, the time-step is computed as for the **standard** scheme defined by equations (10) and (11) already used in [9]:

$$\Delta t = \kappa \min_j \left(\frac{l_j}{c_j} \right) \quad (50)$$

where the lengthscale $l_j = \frac{|\Omega_j|}{\sum_r |\mathbf{C}_{jr}|}$ is the volume over the surface of the cell,

and $\kappa = \frac{1}{2}$ is a safety coefficient.

6.3. Second-order in space extension

The second-order in space extension is formally achieved thanks to a MUSCL-like procedure [48]. Values of the centered unknowns p_j and \mathbf{u}_j are reconstructed using a first-order Taylor-expansion

$$\varphi(\mathbf{x}) \approx \varphi_j + (\nabla \varphi)_j \cdot (\mathbf{x} - \mathbf{x}_j),$$

and their extrapolated values at the vertices r of the mesh are used to compute the fluxes \mathbf{F}_{jrf} and \mathbf{H}_{jrf} . The whole procedure to compute and limit the fluxes is described in [27]. In the tests, we use a Barth-Jespersen-type limiter [4] for scalar, and the adaptation of the VIP limiter described in [35].

7. Numerical illustrations

We propose to assess the method on several test problems. The first-order method is evaluated only on the low-Mach vortex problem 7.1, for information. For all the other problems, we evaluate the robustness and the gain in term of precision for the second-order method. The test 7.2 is a modified Sod shock tube including a stationary flow into the rarefaction fan. The test 7.3 is the famous Noh problem on a Cartesian grid. These two tests are used to assess the robustness of the method in high-Mach configurations. The last two problems 7.4 and 7.5 are designed to evaluate the gain in precision of the method for instability growth calculation, respectively in planar and spherical configurations. All these problems have been run: 1-with the **standard** scheme defined by equations (10), (11), (14) what is referred as **standard** in the results, 2-with the modified scheme defined by equations (35), (33), (34), (49) referred as **emodified** (for modified entropic) in the results, and 3- with the modified scheme defined by equations (35), (33), (34), (48), referred as **bmodified** (for modified basic) in the results. For problems with no analytic solution, a reference is computed with the **standard** scheme on a fine mesh with respect to the Mach number ($\bar{h} < M$), and is referred as **reference**.

7.1. Vortex

We reproduce a test proposed in [15] and also performed in [10]. The flow is defined in $\Omega = [0, 1] \times [0, 1]$ by the initial conditions,

$$\begin{aligned} u(x, y, 0) &= 2 \sin^2(\pi x) \sin(\pi y) \cos(\pi y), \\ v(x, y, 0) &= 2 \sin(\pi x) \cos(\pi x) \sin^2(\pi y), \\ p(x, y, 0) &= 1000, \\ \rho(x, y, 0) &= 1 - \frac{1}{2} \tanh(y - \frac{1}{2}), \end{aligned}$$

and symmetry boundary conditions. These conditions correspond to a Mach number $M \approx 0.027$. The calculation is run until $t = 0.125$.

We have performed a reference study on this test for the first and second-order schemes. For each of these tests, we compute $\mathcal{E}(\Delta x) = |\mathbf{u}^R - \mathbf{u}_{\Delta x}|_{L^2(\Omega)}$, where \mathbf{u}^R corresponds to a calculation with the second-order **standard** scheme on a 1600×1600 cells mesh (corresponding to $\Delta x = 6.25 \times 10^{-4}$), and $\mathbf{u}_{\Delta x}$ to the velocity obtained on a (initially) Cartesian grid of size Δx . These results are displayed in the table 1 and obtained thanks to the post-processing tool *Odace* [2].

As expected, the first-order **standard** scheme fails to predict the correct solution, and even on the finer $\Delta x = 2.5 \times 10^{-3}$ grid, it remains worst than the first-order **bmodified** scheme. Second-order **standard** scheme performs better, but more than respectively two or three grid refinements are necessary to achieve the same precision than respectively the **emodified** or the **bmodified** schemes. That is why we consider that the results obtained on the $\Delta x = 2.5 \times 10^{-3}$ grid with the **emodified** scheme and on the $\Delta x = 10^{-2}$, $\Delta x = 5 \times 10^{-3}$ and $\Delta x = 2.5 \times 10^{-3}$ with the **bmodified** scheme are at least as good as the

Δx	4×10^{-2}	2×10^{-2}	10^{-2}	5×10^{-3}	2.5×10^{-3}
standard					
order 1	2.3×10^{-1}	1.9×10^{-1}	1.5×10^{-1}	1.2×10^{-1}	7.9×10^{-2}
order 2	1.2×10^{-1}	4.9×10^{-2}	2×10^{-2}	7×10^{-3}	2.6×10^{-3}
emodified					
order 1	1.4×10^{-1}	9.6×10^{-2}	6×10^{-2}	3.5×10^{-2}	1.9×10^{-2}
order 2	1.6×10^{-2}	5.7×10^{-3}	2×10^{-3}	1×10^{-3}	8.8×10^{-4}
bmodified					
order 1	2.6×10^{-2}	1.3×10^{-2}	6.5×10^{-3}	3.3×10^{-3}	1.8×10^{-3}
order 2	6.1×10^{-3}	1.6×10^{-3}	8.8×10^{-4}	8.9×10^{-4}	9.2×10^{-4}

Table 1: **Vortex problem**: convergence table. Red values correspond to solutions we consider as good or better than the reference solution on the $\Delta x = 6.25 \times 10^{-4}$ grid.

reference result on the $\Delta x = 6.25 \times 10^{-4}$ grid, which explains the stagnation observed in table 1 (red terms). We also observe that the entropy enforcement for the modified scheme generates a lost of accuracy corresponding to roughly one grid refinement comparing **emodified** with **bmodified**.

To illustrate these results, we display on figure 2 the norm of the velocity map for the 50×50 grid ($|\mathbf{u}|_{\Delta x=2 \times 10^{-2}}$) for the first-order schemes. These results are quite disappointing for the **emodified** scheme, showing that the entropy enforcement leads to a severe lost of precision on this coarse grid.

We display on figure 3 the norm of the velocity map for the 50×50 grid ($|\mathbf{u}|_{\Delta x=2 \times 10^{-2}}$) for the second-order schemes. The lack of precision of the **standard** schemes is still clear, even at second-order, while low-Mach correction allows to recover satisfactory results.

The last diagnostic for this test consists in plotting the velocity norm along the $y = 0.5$ line to observe the convergence to the reference solution. This is displayed on figure 4 for the second-order schemes. It enlightens the interest of the low-Mach correction. It shows also the non-negligible loss of precision for this test, due to the enforcement of the entropy (**emodified** versus **bmodified**).

7.2. Modified Sod shock tube

To now assess the robustness of the method, we run a problem issued from the paper of Thornber *et al* [47]. It consists in a Riemann problem with the following initial conditions:

$$(\rho, u, p)_L = (1, -0.5, 1) \quad (\rho, u, p)_R = (0.125, 0, 0.1) \quad \gamma = 1.4$$

on $\Omega = [0, 1]$.

This test is relevant for low-Mach methods because it includes a stationary flow into the rarefaction fan. It tests the low-Mach correction for unphysical rarefaction shocks when the dissipation becomes low in the fan.

We run the calculation until $t = 0.17$ with the **standard**, **emodified** and **bmodified** schemes with a 100 cells grid (corresponding initially to $\Delta x = 10^{-2}$ for all cells).

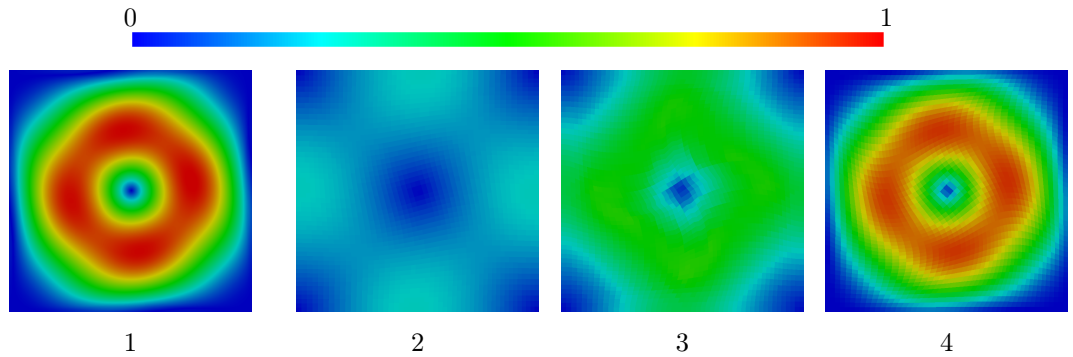


Figure 2: **Vortex problem:** $|u|$ maps 1-reference on a $\Delta x = 6.25 \times 10^{-4}$ grid, 2-**standard first-order scheme** on a $\Delta x = 2 \times 10^{-2}$ grid, 3-**emodified first-order scheme** on a $\Delta x = 2 \times 10^{-2}$ grid and 4-**bmodified first-order scheme** on a $\Delta x = 2 \times 10^{-2}$ grid. On coarse grids, We notice the distortion of the grid due to the Lagrangian framework of the calculations. Structure of the solution is completely lost with the **standard** first-order scheme and almost lost with the **emodified** first-order scheme on this grid. Only the **bmodified** first-order scheme succeed in providing a decent result.

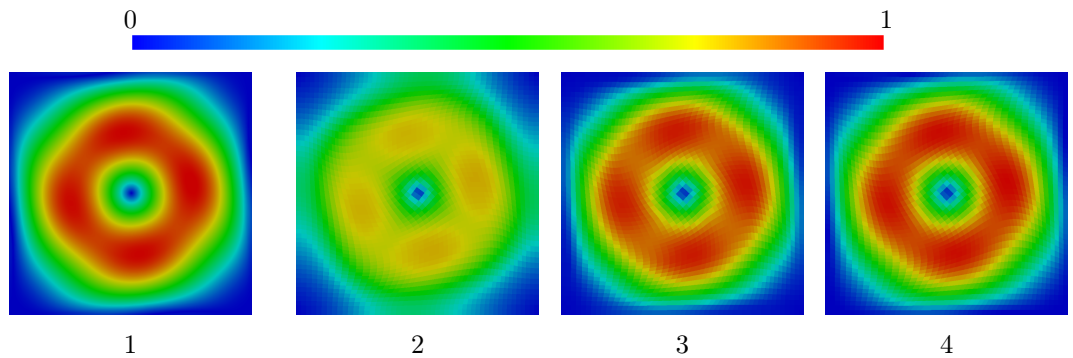


Figure 3: **Vortex problem:** $|u|$ maps 1-reference on a $\Delta x = 6.25 \times 10^{-4}$ grid, 2-**standard second-order scheme** on a $\Delta x = 2 \times 10^{-2}$ grid, 3-**emodified second-order scheme** on a $\Delta x = 2 \times 10^{-2}$ grid and 4-**bmodified second-order scheme** on a $\Delta x = 2 \times 10^{-2}$ grid. Structure of the solution is hardly distinguishable with the the **standard** scheme. The **emodified** and **bmodified** schemes gives visually good results.

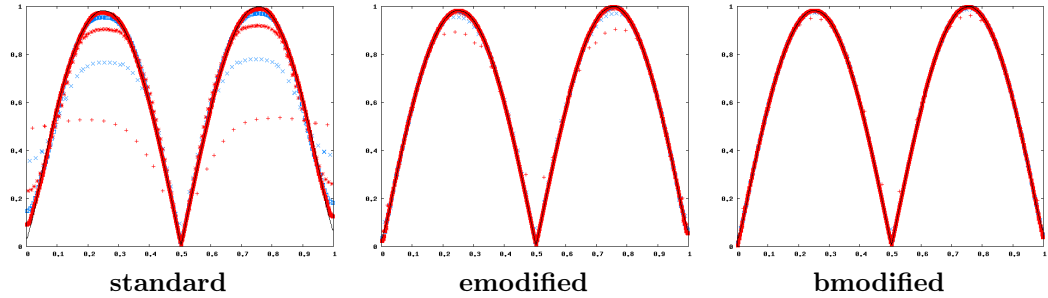


Figure 4: **Vortex problem:** $|u|$ plots along $y = 0.5$ line. $+$: $\Delta x = 4 \times 10^{-2}$ grid, \times : $\Delta x = 2 \times 10^{-2}$ grid, $*$: $\Delta x = 10^{-2}$ grid, \square : $\Delta x = 5 \times 10^{-3}$ grid, \blacksquare : $\Delta x = 2.5 \times 10^{-3}$ grid, $-$ reference on the $\Delta x = 6.25 \times 10^{-4}$ grid. The **standard** scheme curves does not match the finer mesh curve, even with the $\Delta x = 2.5 \times 10^{-3}$ mesh, while **emodified** and **bmodified** scheme curves match the reference respectively from the $\Delta x = 10^{-2}$ grid and $\Delta x = 2 \times 10^{-2}$ grid.

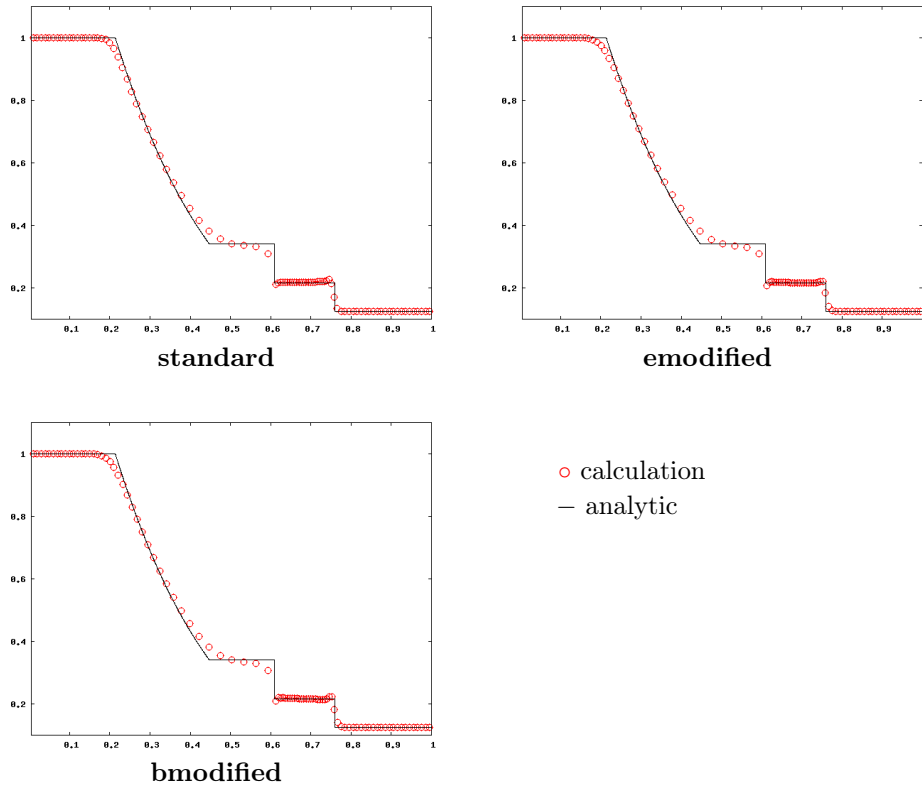


Figure 5: **Shock tube problem:** Plots of ρ along x for the second-order versions of the schemes. Sensitivity with respect to the low-Mach correction is weak for this test, assessing the robustness of the method even in stationary configurations.

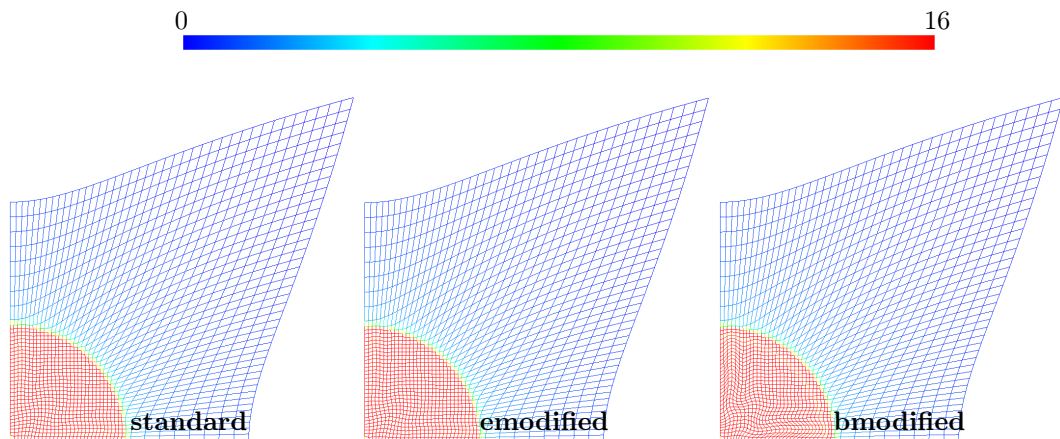


Figure 6: **Noh problem**: Mesh and density fields at the final time. Results are satisfactory for all versions of the scheme. However, the grid obtained with the **bmodified** scheme is more deformed than the other ones, what is related to an entropy defect.

Results are displayed on figure 5. It shows that the results in term of robustness are not affected by the low-Mach correction. The fan profile is also unaffected by the stationary flow condition, what was expected since the schemes respect the Galilean invariance.

7.3. Cylindrical Noh problem on Cartesian grid

We perform a cylindrical Noh [42] calculation on a 50^2 Cartesian grid. Initial conditions consists in a density $\rho = 1$ in the entire domain, and an inward velocity of magnitude 1. The initial domain size is 1^2 . Initial pressure is theoretically zero, but we use the classical value $p = 10^{-6}$ leading to a very low initial sound-speed and a large Mach number $\frac{1}{c} = M \approx 775$. This test is challenging for low-Mach correction, because the Mach number varies theoretically through the shock from infinity to zero (and with our numerical setting from 775 to zero). We run the problem until $t = 0.6$. We depict on figure 6 the final grids obtained with the three - **standard**, **emodified** and **bmodified** - second-order schemes. Colors correspond to the density field.

We also plot on figure 7 the average density in all the cells at the final time versus the radius for the three versions of the scheme. The results obtained with the **emodified** and **bmodified** versions are close to the one obtained with the **standard** scheme. However, wiggles appear in the solution in using the non-entropic **bmodified** schemes. These wiggles disappear in enforcing the entropy of the scheme (**emodified** version).

This test assess the robustness of the method in strong shock configurations corresponding to a Mach number ranging from zero to «infinite».

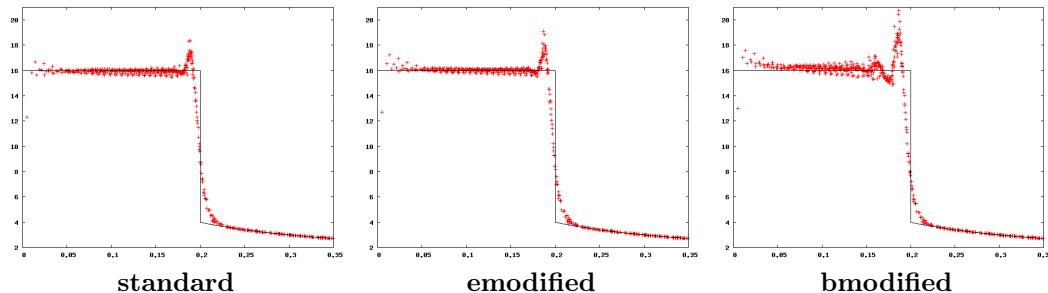


Figure 7: **Noh problem**: density versus radius in all cells. $+$: numerical result, $-$ analytical solution. The result with the **bmodified** scheme is quite noisy. This defect is cured in using the entropic version **emodified**.

7.4. Planar flow Richtmyer-Meshkov instability

We aim at quantifying the effect of the low Mach correction for hydrodynamic instability calculations in converging configuration. An intermediate step to achieve this goal consist in evaluating this effect on planar configurations (meaning that the mean flow is 1D planar). Since during an implosion the material interfaces can lie into both high-Mach or low-Mach region depending on the time, we have performed a study to determine the effect of the correction for several Mach number. We focus on the Richtmyer-Meshkov instability [44], which occurs when a shock hits a perturbed interface. For sufficiently small initial perturbation, it leads to an asymptotic linear growth of the perturbation amplitude with time (called terminal growth rate). This terminal growth can be estimated thanks to linear perturbation theory. Some authors [14, 49, 50] have indexed the terminal growth rates in a table for different adimensional initial conditions. The relevant parameters for this problems are the initial density ratio of the fluids, the shock strenght depending on the pressure ratio between shocked and at rest fluid, and by the adiabatic constant of the two fluids. We have performed several calculations for different initial conditions in order to estimate the effect of the low-Mach correction. Our conclusion is that under $M \approx 0.3$, revelant improvement on the solution can be made using the low-Mach correction. Obviously, these improvements become more signifiant when the Mach number get smaller. To illustrate this statement, we propose to report on two different Mach configurations for which the terminal growth rate of the Richmyer-Meshkov instability is available in the litterature. The first-one correspond to a medium Mach number $M \approx 0.5$, the second-one to a low Mach number $M \approx 3 \times 10^{-2}$. We use the same $[-5 \ 4.2] \times [0 \ \lambda/2]$ rectangular computational domain for both problems, with $\lambda = 1$ and $\alpha_0 = 10^{-3}$ corresponding respectively to the wavelenght and the initial amplitude of the perturbation. No flow boundary conditions are applied in $y = 0$, $y = 1/2$ and $x = 4.2$. We use three different grid refinements. The coarser is a 460×25 uniform grid as in [38]. Then we refine in the two direction to obtain the second (960×50) and the third (1920×100) grids. We have verified that the mean flow calculation is

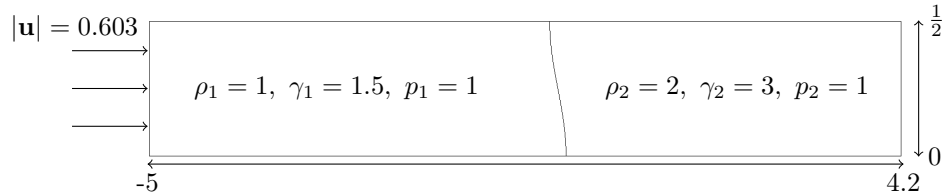


Figure 8: **Planar $M \approx 0.5$ instability:** domain and initial conditions. The perturbation has been artificially amplified ($a_0 = 0.1$) for visualization purpose.

already converged with the coarse grid.

$M \approx 0.5$ configuration. The parameters for this simulation are the same as those of [38] and are illustrated by the figure 8. It corresponds to a density ratio $\rho_2/\rho_1 = 2$ and a shock strength of $s = 1 - p_1/p_1^s = 0.5$, where p_1^s accounts for the pressure of the shocked fluid 1. For this configuration, tables (we choose the one in [14], but all references are very close) give us an adimensional terminal growth rate of 0.0635 which corresponds to a dimensional growth rate of 0.6616. The calculation is run until $t = 6.5$, while the time for which the shock hits the interface is $t \approx 3.015$.

We have compared the adimensional perturbation amplitude versus time profiles obtained with the different second-order schemes, which are displayed on figure 9. It is shown that the low-Mach correction has almost no influence at this regime. However, it does not impact negatively the robustness of the calculation.

$M \approx 0.03$ configuration. The parameters for this simulation are illustrated by the figure 8. It corresponds to a density ratio $\rho_2/\rho_1 = 2$ and a shock strength of $s = 1 - p_1/p_1^s = 0.05$ (weak shock), where p_1^s accounts for the pressure of the shocked fluid 1. For this configuration, tables (we choose the one in [14], but all references are very close) give us an adimensional terminal growth rate of 0.00725 which corresponds to a dimensional growth rate of 0.1603. The calculation is run until $t = 3.5$, while the time for which the shock hits the interface is $t \approx 1.403$.

We have compared the adimensional perturbation amplitude versus time profiles obtained with the different second-order schemes, which are displayed on figure 11. It is shown that the low-Mach correction improve widely the results at this regime. Growth rate prediction is almost the same for the **emodified** and **bmodified** schemes, but some wiggles appear with the **bmodified** scheme when the shock hits the interface. We also display the same plots for the 100 cells per wavelength (figure 12). Conclusions are the same.

7.5. Convergent flow instability

We now estimate the effect of this modification on convergent flows, and in particular, convergent flows in a configuration for which the initial Mach

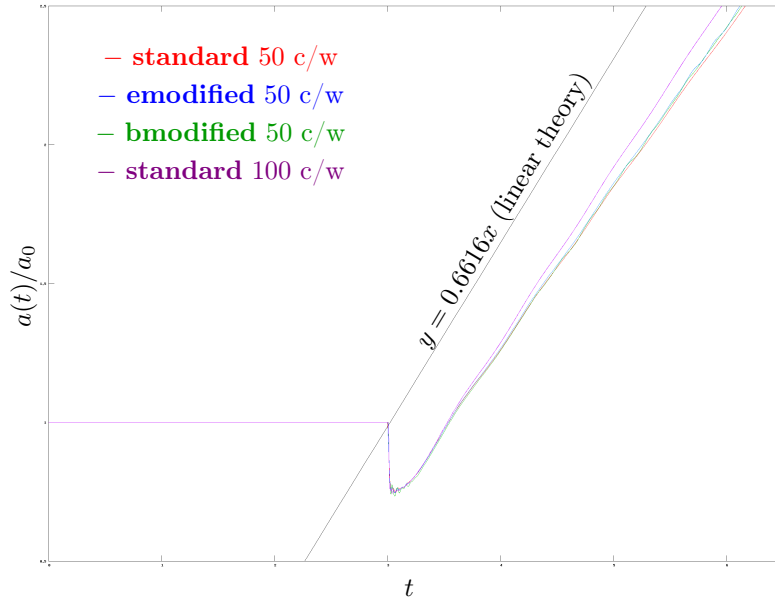


Figure 9: **Planar $M \approx 0.5$ instability:** adimensional amplitude versus time (c/w stands for cells per wavelength). A very small improvement of the growth rate estimation is obtained with the low-Mach correction (**emodified** and **bmodified** versus **standard**) on the 50 cells per wavelength grid. The result is by far more improved in refining (100 cells per wavelength) the grid. Note that **emodified** and **bmodified** schemes give almost the same answer.

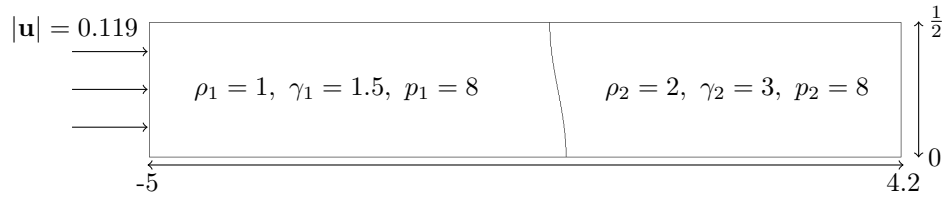


Figure 10: **Planar $M \approx 3 \times 10^{-2}$ instability:** Domain and initial conditions. The perturbation has been artificially amplified ($a_0 = 0.1$) for visualization purpose.

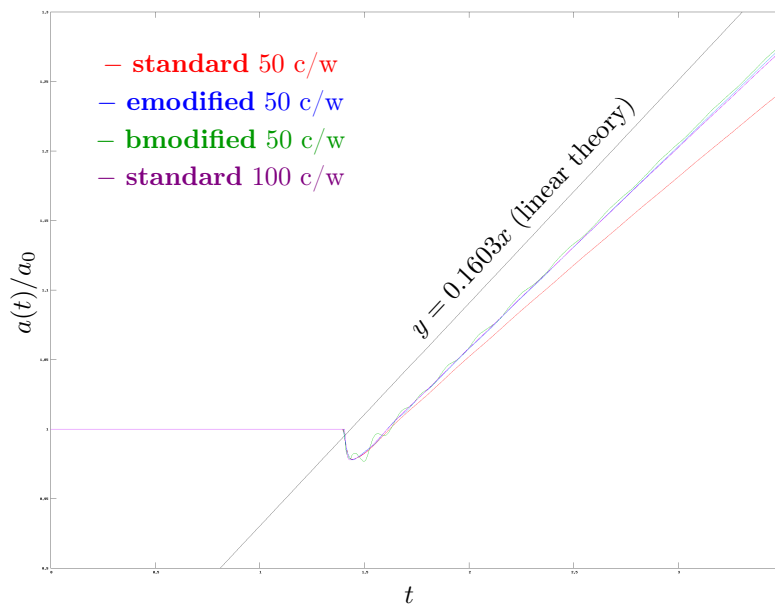


Figure 11: **Planar $M \approx 3 \times 10^{-2}$ instability:** adimensional amplitude versus time (c/w stands for cells per wavelength). Result are widely improved concerning the growth rate estimation with the low-Mach correction (**emodified** and **bmodified** versus **standard**) on the 50 cells per wavelength grid. The results are even better than those of the **standard** scheme on a finer (100 cells per wavelength) grid. Note that **emodified** and **bmodified** schemes give almost the same answer, except some wiggles just after the shock hits the interface for the **bmodified** scheme.

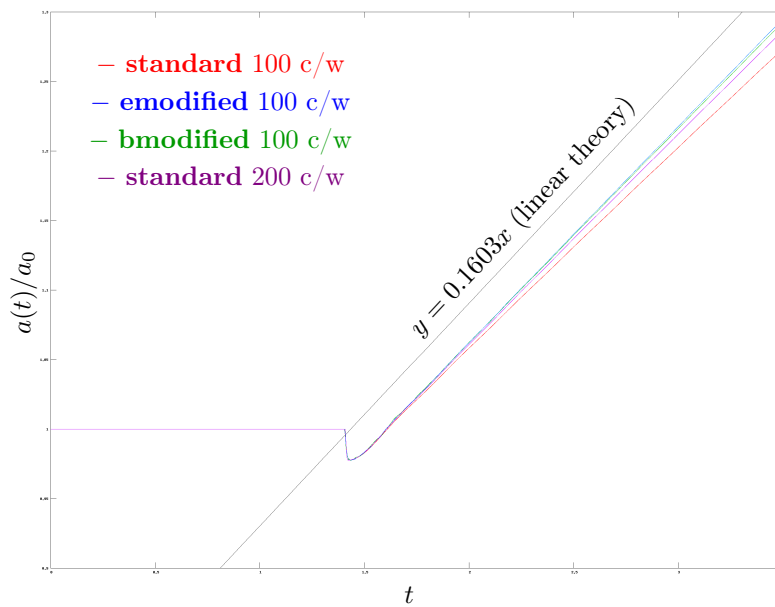


Figure 12: Adimensional amplitude versus time for the $M \approx 0.03$ Richtmyer-Meshkov instability problem (c/w stands for cells per wavelength). Results are widely improved concerning the growth rate estimation with the low-Mach correction (**emodified** and **bmodified** versus **standard**) on the 100 cells per wavelength grid. The results are even better than those of the **standard** scheme on a finer (200 cells per wavelength) grid. Note that **emodified** and **bmodified** schemes give almost the same answer, except some wiggles just after the shock hits the interface for the **bmodified** scheme.

number is high. However, it decreases during the calculation because of the implosion framework. The kind of applications we are interested in, consists in a high kinetic energy and high density shell imploding on a light gaz cavity, as for instance for Ignition Confinement Fusion (ICF) target. However, we widely simplify the problem in considering only one initial contact discontinuity in our study -ICF targets are composed of at least three layer: a outer plastic shell, a inner iced DT shell, and a gaz DT central cavity- in order to ease the interpretation of the results. This simplification has obviously a big impact on the global dynamic of the flow. However, we constructed this problem in order to approximatively respect mass ratio between light and heavy material, and adimensional heavy shell velocity. The initial conditions of the problem are reported on figure 13. The second-order version of the scheme is used for all the calculations.

Meshing. We perform the calculation in cylindrical $r - z$ geometry, on a half-sphere. Symmetry boundary conditions are applied on the r and z axis. Since there is no analytical solution for this problem, we perform a convergence study. We propose five grids (M1 to M5). As depicted in figure 13, we use an equal angle zoned polar grid for the shell Ω_H . Ω_l is divided into two parts. The central part is meshed with an O-grid, and the outer part is meshed with a polar grid. The O-grid is constructed so that the axis r and z have a uniform cutting without perturbation.

For the coarsest M1 grid, the shell is paved with 30 slices and 40 uniform layers so that the initial layer thickness is $\Delta_{M1} = 2.5 \times 10^{-3}$. The size of the center box of the cavity is 0.15^2 , paved with 15^2 squares. Then, 30 layers are used for the remaining of the cavity grid. M2, M3, M4 and M5 grids are obtained in multiplying respectively by a factor of 2, 4, 8 and 16, the number of cells of the grid M1 in the r and z directions. The initial layer thicknesses Δ_{M2} , Δ_{M3} , Δ_{M4} and Δ_{M5} of the grids M2, M3, M4 and M5 are consequently divided by a factor 2, 4, 8 and 16.

We call Γ the interface between the shell Ω_H and the cavity Ω_l . Initial mean radius of Γ is called $R_\Gamma = 0.45$.

Numerical parameters.

- The calculation is run until $t = 0.06$.
- The area-weighted formulation of the Eucclhyd scheme (refer to [37]) is used to perform this calculation.
- Small amount of subzonal entropy [21] is applied at the vicinity of the outer boundary of the shell, in order to prevent spurious deformations of this interface during the unstable phase.
- The convergence study is performed with the **standard** scheme.

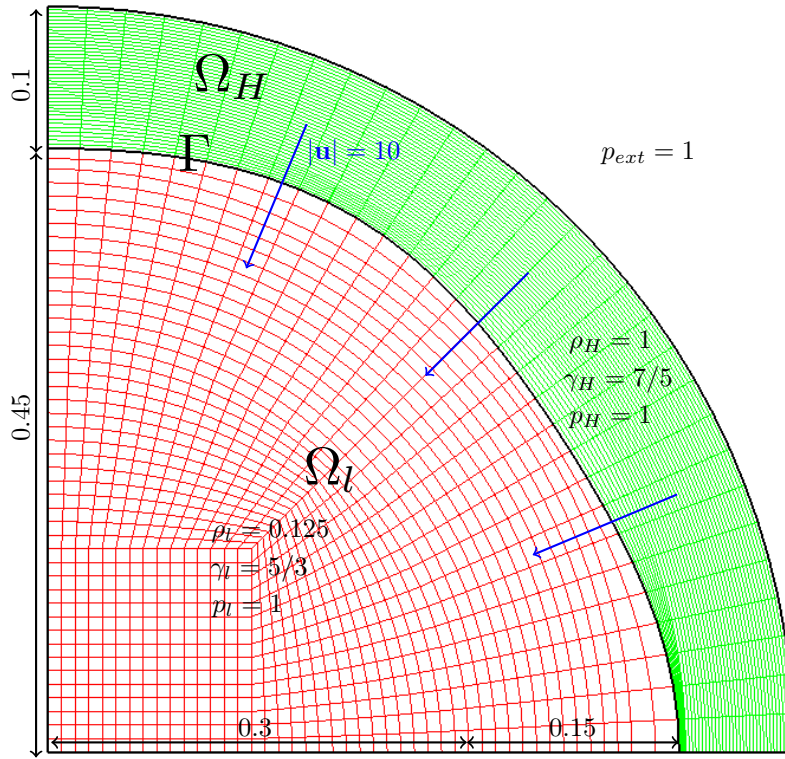


Figure 13: **Spherical instability problem:** initial M1 grid and conditions. Black line accounts for the interface Γ between the shell Ω_H and the cavity Ω_l . Amplitude of the perturbation on Γ has been increased to $a_0 = 1.5 \times 10^{-2}$ for visualization purpose. The dimensions correspond to an unperturbed configuration.

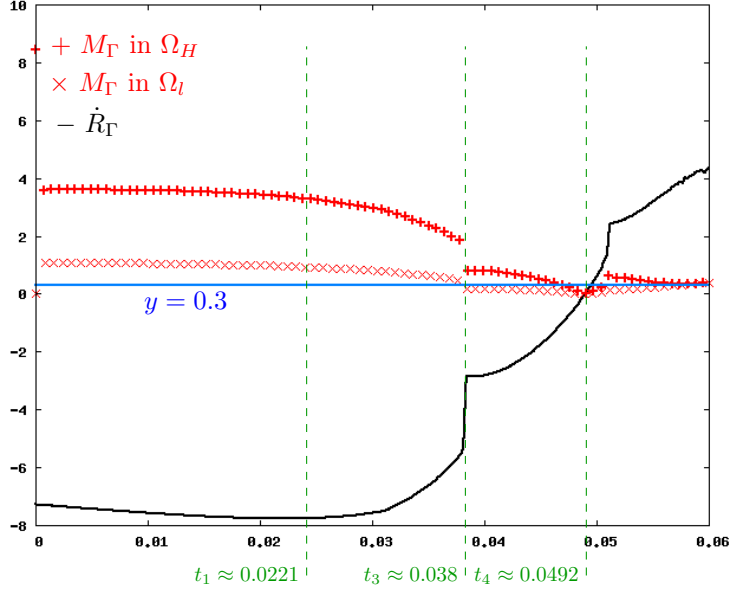


Figure 14: **Spherical instability problem:** velocity profile. The red symbols $+$ and \times stand for the Mach number at the vicinity of Γ , respectively in the heavy Ω_H fluid, and in the light Ω_l fluid at the orthoradial position $\theta = \pi/4$. Blue lines represent the value of M below which the flow can be considered to be low-Mach ($M < 0.3$).

Mean flow description. Now, we briefly describe the main features of the mean flow.

The interface speed magnitude slowly increases at the beginning of the calculation due to confinement. A detached shock compressed the gas in the cavity ahead of the interface. About $t_1 \approx 0.0221$, pressure inside the cavity becomes higher than in the shell, and the velocity of the interface decreases. This is the end of the stable phase. The detached shock focus at $t_2 \approx 0.028$ and bounces. Then, it diverges and crosses the interface at $t_3 \approx 0.038$. The expansion phase (outward mean velocity for the interface) begins at time $t_4 \approx 0.0492$. Minimum mean radius of the interface is $R_\Gamma^{\min} \approx 0.145$. Mean velocity $\dot{R}_\Gamma(t)$ versus time is displayed on figure 14.

We provide in figure 15 1D plots of the radius versus time. It demonstrates that the mean flow is almost converged on the coarsest mesh M1 (for instance, minimal volume of the cavity on M1 is 6.67×10^{-2} , while a Richardson extrapolation [43] gives a converged minimal volume of 6.6×10^{-2}).

Perturbation description. Our goal is to compare the growth rate of an instability with and without the low-Mach correction. To this aim, we apply a perturbation on the interface Γ . For a sphere in cylindrical geometry, the relevant frame for perturbation analysis is the Legendre frame (more details on Legendre frame can be found for instance in [12]). Since we perform the calculation on a

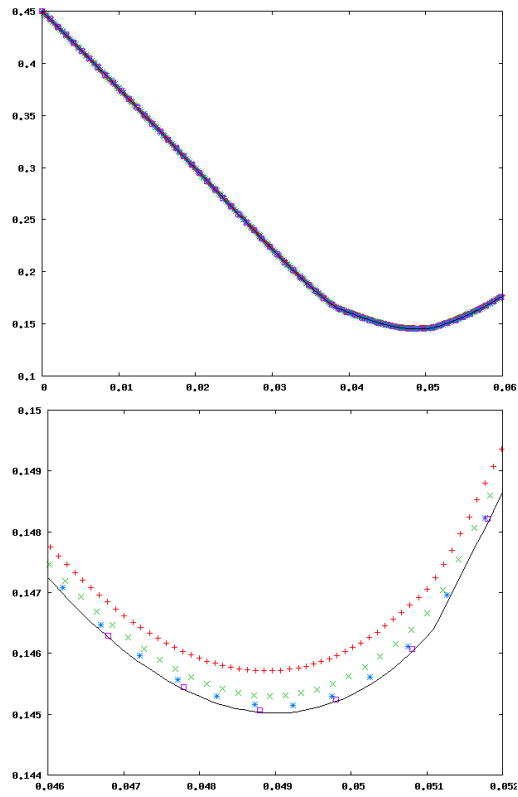


Figure 15: **Spherical instability problem:** left part of the figure: 1D plot of the mean interface radius $R_\Gamma(t)$ versus time. Right part of the figure: zoom around minimum mean radius time t_4 . + M1 (coarsest) grid; \times M2 grid; $*$ M3 grid; \square M4 grid; $-$ M5 (finest) grid simulation.

half-sphere, only even modes can grow. We choose a mode 6. It means that the positions of the interface nodes is computed initially by:

$$\begin{cases} r &= R_\Gamma \cos \theta + a_0 P_6(\cos \theta) \\ z &= R_\Gamma \sin \theta + a_0 P_6(\sin \theta) \end{cases}$$

where θ is the angle between the $(r, z)^T$ vector and the z axis, P_6 the 6th Legendre polynomial, and a_0 the initial amplitude of the perturbation. In this work, we choose $a_0 = 10^{-4}$. Consequently, since $0.1 \times R_\Gamma/6 = 0.0075 > 10^{-4}$ (refer for instance to [26]), the perturbation growth can be considered as linear at the beginning of the calculation. This linear behaviour allows systematic comparisons, what will be much more difficult for a non-linear perturbation growth. Because of the initial shock (refer to the mean flow description), the perturbation grows due to Richtmyer-Meshkov instability [44] until $t_1 \approx 0.0221$. Then, the flow is Rayleigh-Taylor unstable [46].

Instability growth. We first check that the instability growth remains essentially linear during the whole calculation. The amplitude versus time of even modes from 2 to 18, in term of normalized power $W_l = a_l^2(t)/a_0^2$ (where a_l stands for the amplitude of the mode l), is displayed on figure 16. These results are obtained with the **standard** scheme on the M5 finest grid. The amplitudes of all the modes except a_6 remains below a_0 . Consequently, we consider that we are in the linear regime during the whole calculation.

On the figure 17, we display a plot of the normalized power of the mode 6, W_6 , for all the grids M1 to M5. It shows that this quantity is almost converged on M5. At the time $t = 0.055$, a Richardson extrapolation gives $575 \leq W_6 \leq 585$, depending on the grids considered to perform the extrapolation (the asymptotic regime of the extrapolation is not reached).

Effect of the low-Mach correction. We now investigate the effect of the low-Mach correction for this problem. We insist on the fact that this problem can not be considered at all as a low-Mach problem, since the initial Mach number at the interface Γ , $M_\Gamma^{\text{init}} \approx 2.5$. However, since it is convergent problem, interface undergoes briefly a low-Mach regime between $t_3 \approx 0.038$ and $t \approx 0.058$ (refer to figure 14). In the following, we display only the results with the **modified** scheme. We have checked that the main flow results are unaffected by the low-Mach correction. We display on figure 18, the comparison between the **standard** and the **modified** scheme in term of W_6 versus time on the coarsest M1 grid. It shows that despite the fact that the interface Γ undergoes only briefly a low-Mach regime, it has an undeniable impact on the precision of the calculation of the instability. However, this impact does not compensate a coarsening of a factor of 2 in all the directions (the **standard** scheme on M2 remains more precise than the **modified** scheme on M1). Looking more carefully at the local dynamic of the perturbation growth, we observe on the central part of figure 18, that at $t = t_3 = 0.038$, the curves corresponding to the **standard** scheme and to the **modified** scheme almost coincide on M1 grid. As a matter of fact, Γ does not stand in a low-Mach region before this time.

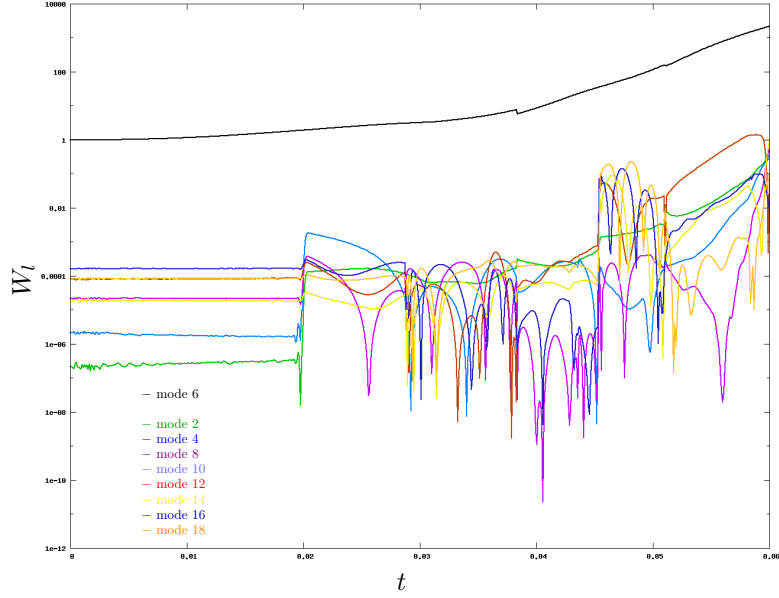


Figure 16: **Spherical instability problem:** normalized power $W_i = a_i^2(t)/a_0^2$ of the amplitudes of the even modes of the perturbation versus time for the **standard** scheme on the M5 finest grid.

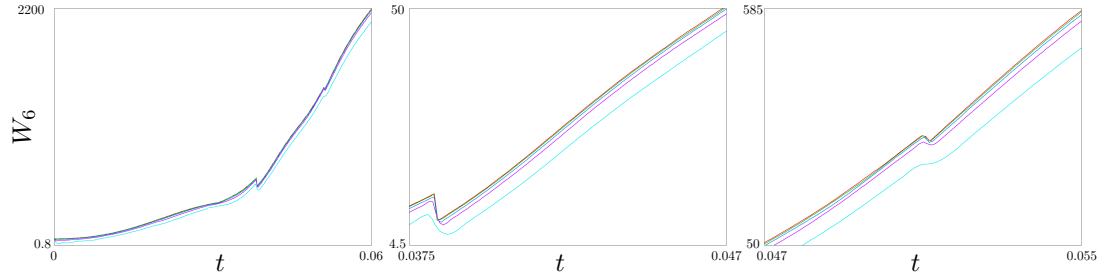


Figure 17: **Spherical instability problem:** normalized power $W_6 = a_6^2(t)/a_0^2$ of the amplitude of the mode 6 of the perturbation versus time for the **standard** scheme. Convergence study: — M1 (coarsest) grid, — M2 grid, — M3 grid, — M4 grid, — M5 (finest) grid. Left figure displays the whole time of the calculation. Central figure displays the times between $t = 0.00375 \approx t_3$ until $t = 0.047$. Right figure displays times between $t = 0.047$ until $t = 0.055$ (around t_4).

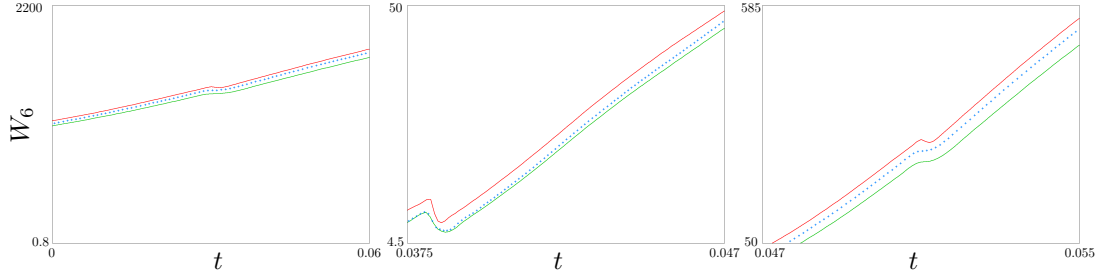


Figure 18: **Spherical instability problem**: normalized power $W_6 = a_6^2(t)/a_0^2$ of the amplitude of the mode 6 of the perturbation versus time. Comparisons: — **standard** scheme on the M1 (coarsest) grid, + **modified** scheme on the M1 grid, — **standard** scheme on the M2 grid. Left figure displays the whole time of the calculation. Central figure displays the times between $t = 0.00375 \approx t_3$ until $t = 0.047$. Right figure displays times between $t = 0.047$ until $t = 0.055$ (around $t_4 = 0.0492$).

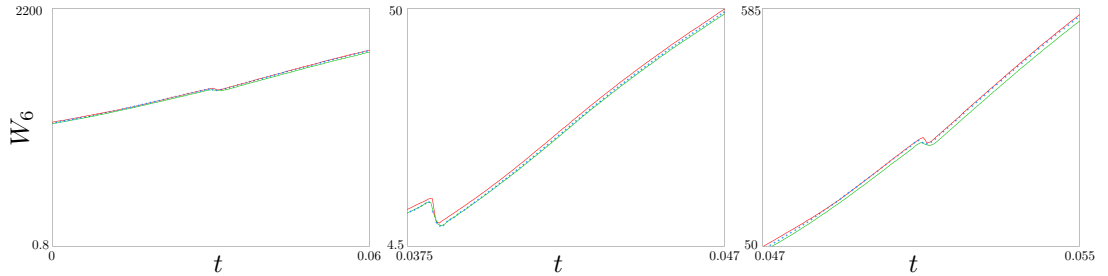


Figure 19: **Spherical instability problem**: normalized power $W_6 = a_6^2(t)/a_0^2$ of the amplitude of the mode 6 of the perturbation versus time. Comparisons: — **standard** scheme on the M2 grid, + **modified** scheme on the M2 grid, — **standard** scheme on the M3 grid. Left figure displays the whole time of the calculation. Central figure displays the times between $t = 0.00375 \approx t_3$ until $t = 0.047$. Right figure displays times between $t = 0.047$ until $t = 0.055$ (around $t_4 = 0.0492$).

It is only for $t > t_3$, that the perturbation growth is sensitive to the low-Mach correction (right parts of figure 18). Same analysis can be made on finer grids, as displayed on figure 19 for the M2 grid. The enhancement obtained with the low-Mach correction for this problem can be considered as small. However, a coarser mesh ($\approx \times 0.65$ per direction) is sufficient to reach an equivalent precision with the **standard** scheme for the growth rate of the perturbation, and since the low-Mach correction has no impact on the cost of the calculation, it corresponds roughly to a save of CPU times of 75% in 2D and 85% in 3D for an equivalent precision on the W_6 profile for this problem. Obviously, this gain is problem dependant, but we insist on the fact that the configuration we have chosen can not be considered at all as a low-Mach problem.

8. Conclusion

In this work, we have studied the low-Mach regime for acoustic-Godunov solvers for the multi-D Euler equations in Lagrangian frame. We have analytically explained why standard solvers suffer a drastic loss of precision at low-Mach number. We have proposed a modification to the solver, very easy to implement and computationally costless. This modification consists mainly in performing a convex combination of the fluxes involving two parts: first one corresponds to the standard fluxes, and second one to centered fluxes. The coefficients of the convex combination depend on the Mach number. We have demonstrated that this modification cures the standard solver deficiencies at low-Mach number, and shows that it is not contradictory with the entropy stability criterion. We propose a formula for these coefficients. A second-order extension of this scheme has been proposed. The modified scheme has been implemented and assessed on several test problems. This numerical study shows that it succeeds in widely increasing the precision for low-Mach problems, and it remains as precise and robust as the standard scheme in high-Mach regime, even at high order. We finally showed that, on a convergent instability growth problem, this modification can perceptibly enhance the results, even for high-velocity flows. A natural following of this work could consist in evaluating the effect of replacing the centered part of the fluxes with isentropic fluxes (refer to [7, 39]).

Acknowledgement

The author thanks Agnès Grenouille for her help in the post-treatment of the data. Many thanks to Gilles Carré, Mathieu Girardin and Stéphane Del Pino for fruitful discussions about this work.

- [1] F. L. Addessio, J. R. Baumgardner, Dukowicz, N. L. J. K., Johnson, B. A. Kashiwa, R. M. Rauenzahn, and C. Zemach. CAVEAT: A Computer Code for Fluid Dynamics Problems with Large Distortion and Internal Slip. Technical report, Los Alamos National Laboratory LA-10613, 1990.
- [2] D. Aguilera, Th. Carrard, C. Guilbaud, J. Schneider, and S. Sorbet. Visualization and post-processing for high performance computing. *Chocs*, 41:57–67, 2012. In french.
- [3] Andrew J. Barlow, Pierre-Henri Maire, William J. Rider, Robert N. Rieben, and Mikhail J. Shashkov. Arbitrary Lagrangian Eulerian methods for modeling high-speed compressible multimaterial flows. *Journal of Computational Physics*, 322:603 – 665, 2016.
- [4] T. Barth and D. Jespersen. The design and application of upwind schemes on unstructured meshes. in *aiaa paper 89-0366*. In *27th Aerospace Sciences Meeting*, Reno, Nevada, 1989.
- [5] D. J. Benson. Computational methods in Lagrangian and Eulerian hydrocodes. *Comp. Meth. Appl. Mech. Eng.*, 99:235–394, 1992.

- [6] Jean-Christophe Boniface. Rescaling of the Roe scheme in low Mach-number flow regions. *Journal of Computational Physics*, 328:177 – 199, 2017.
- [7] Jean-Philippe Braeunig. Reducing the entropy production in a collocated Lagrange-Remap scheme. *Journal of Computational Physics*, 314:127 – 144, 2016.
- [8] D. Burton, T. Carney, N. Morgan, S. Sambasivan, and M. Shashkov. A cell-centered Lagrangian Godunov-like method for solid dynamics. *Comput. Fluids*, 83:33–47, 2013.
- [9] G. Carré, S. Del Pino, B. Després, and E. Labourasse. A cell-centered Lagrangian hydrodynamics scheme on general unstructured meshes in arbitrary dimension. *J. Comput. Phys.*, 228:5160–5183, 2009.
- [10] C. Chalons, M. Girardin, and S. Kokh. An All-Regime Lagrange-Projection Like Scheme for the Gas Dynamics Equations on Unstructured Meshes. *Commun. Comput. Phys.*, 20:188–233, 2016.
- [11] Christophe Chalons, Mathieu Girardin, and Samuel Kokh. An all-regime lagrange-projection like scheme for 2d homogeneous models for two-phase flows on unstructured meshes. *Journal of Computational Physics*, 335:885 – 904, 2017.
- [12] S. Chandrasekhar. *Radiative transfer*. (International Series of Monographs on Physics) Oxford: Clarendon Press; London: Oxford University Press. XIV, 394 p. , 1950.
- [13] J. Cheng and C.-W. Shu. Positivity-preserving lagrangian scheme for multi-material compressible flow. *Journal of Computational Physics*, 257(PA):143–168, 2014.
- [14] Jean-Marie Clarisse, Stéphane Jaouen, and Pierre-Arnaud Raviart. A godunov-type method in lagrangian coordinates for computing linearly-perturbed planar-symmetric flows of gas dynamics. *Journal of Computational Physics*, 198(1):80 – 105, 2004.
- [15] Ph. Colella and K. Pao. A projection method for low speed flows. *J. Comput. Phys.*, 142:245–269, 1999.
- [16] F. Cordier, P. Degond, and A. Kumbaro. An Asymptotic-Preserving all-speed scheme for the Euler and Navier-Stokes equations. *J. Comput. Phys.*, 231:5685–5704, 2012.
- [17] Pierre Degond, S Jin, and J Yuming. Mach-number uniform asymptotic-preserving gauge schemes for compressible flows. *Bulletin-Institute of Mathematics Academia Sinica*, 2(4):851, 2007.

- [18] S. Dellacherie. Analysis of Godunov type schemes applied to the compressible Euler system at low Mach number. *J. Comput. Phys.*, 229:978–1016, 2010.
- [19] S. Dellacherie, J. Jung, P. Omnes, and P.-A. Raviart. Construction of modified godunov-type schemes accurate at any mach number for the compressible euler system. *Mathematical Models and Methods in Applied Sciences*, 26(13):2525–2615, 2016.
- [20] B. Després. Weak consistency of the cell-centered glace scheme on general meshes in any dimension. *Comp. Meth. Appl. Mech. Eng.*, 199:2669–2679, 2010.
- [21] B. Després and E. Labourasse. Stabilization of cell-centered compressible Lagrangian methods using subzonal entropy. *J. Comp. Phys.*, 231(20):6559–6595, 2012.
- [22] B. Després and C. Mazeran. Lagrangian gas dynamics in 2D and lagrangian systems. *Arch. Rat. Mech. Anal.*, 178:327–372, 2005.
- [23] Q.-W. Ge. High-order lagrangian cell-centered conservative scheme on unstructured meshes. *Applied Mathematics and Mechanics (English Edition)*, 35(9):1203–1222, 2014.
- [24] Gilles Gropellier and Benoit Lelandais. The arcane development framework. In *Proceedings of the 8th Workshop on Parallel/High-Performance Object-Oriented Scientific Computing*, POOSC '09, pages 4:1–4:11, New York, NY, USA, 2009. ACM.
- [25] H. Guillard and A. Murrone. On the behavior of the upwind scheme in low Mach number limit, ii. *Comput. Fluids*, 33:655–675, 2004.
- [26] S. Haan. Onset of nonlinear saturation for Rayleigh-Taylor growth in the presence of a full spectrum of modes. *Phys. Rev. A*, 39(11):5812–5824, 1988.
- [27] P. Hoch and E. Labourasse. A frame invariant and maximum principle enforcing second-order extension for cell-centered ALE schemes based on local convex-hull preservation. *Int. J. Numer. Meth. Fluids*, 76:1043–1063, 2014.
- [28] Sergiu Klainerman and Andrew Majda. Singular limits of quasilinear hyperbolic systems with large parameters and the incompressible limit of compressible fluids. *Communications on Pure and Applied Mathematics*, 34(4):481–524, 1981.
- [29] Sergiu Klainerman and Andrew Majda. Compressible and incompressible fluids. *Communications on Pure and Applied Mathematics*, 35(5):629–651, 1982.

- [30] R. Klein. Semi-implicit extension of a godunov-type scheme based on low mach number asymptotics i: One-dimensional flow. *Journal of Computational Physics*, 121(2):213 – 237, 1995.
- [31] X. Li and C. Gu. An All-Speed Roe-type scheme and its asymptotic analysis of low-Mach number behaviour. *J. Comput. Phys.*, 227:5144–5159, 2008.
- [32] M.-S. Liou. A sequel to AUSM, Part II: AUSM⁺-up for all speeds. *J. Comput. Phys.*, 214:137–170, 2006.
- [33] Y. Liu, W. Shen, B. Tian, and D.-K. Mao. A two dimensional nodal riemann solver based on one dimensional riemann solver for a cell-centered lagrangian scheme. *Journal of Computational Physics*, 284:566–594, 2015.
- [34] R. Loubère, P.-H. Maire, and B. Rebourecet. Chapter 13 - staggered and colocated finite volume schemes for lagrangian hydrodynamics. In Rémi Abgrall and Chi-Wang Shu, editors, *Handbook of Numerical Methods for Hyperbolic Problems Basic and Fundamental Issues*, volume 17 of *Handbook of Numerical Analysis*, pages 319 – 352. Elsevier, 2016.
- [35] G. Luttwak and J. Falcovitz. Slope limiting for vectors: A novel vector limiting algorithm. *Int. J. Numer. Meth. Fluids*, 65:1365–1375, 2011.
- [36] P. H. Maire, R. Abgrall, J. Breil, and J. Ovadia. A cell-centered lagrangian scheme for 2D compressible flow problems. *Siam J. Sci. Comp.*, 29, 2007.
- [37] P.H. Maire. A high-order cell-centered Lagrangian scheme for compressible fluid flows in two-dimensional cylindrical geometry. *J. Comput. Phys.*, 228(18):6882–6915, 2009.
- [38] P.H. Maire. A high-order cell-centered Lagrangian scheme for two-dimensional compressible fluid flows on unstructured meshes. *J. Comput. Phys.*, 228(7):2391–2425, 2009.
- [39] C. Mazeran. *Sur la structure mathématique et l’approximation numérique de l’hydrodynamique lagrangienne bidimensionnelle*. PhD thesis, Université de Bordeaux I, November 2007.
- [40] Yann Moguen, Simon Delmas, Vincent Perrier, Pascal Bruel, and Erik Dick. Godunov-type schemes with an inertia term for unsteady full mach number range flow calculations. *Journal of Computational Physics*, 281:556 – 590, 2015.
- [41] J. von Neumann and R. D. Richtmyer. A method for the calculation of hydrodynamics shocks. *J. appl. Phys.*, 21:232–237, 1950.
- [42] W. F. Noh. Errors for calculations of strong shocks using artificial viscosity and an artificial heat flux. *J. Comput. Phys.*, 72:78–120, 1987.

- [43] L. F. Richardson. The approximate arithmetical solution by finite differences of physical problems involving differential equations, with an application to the stresses in a masonry dam. *Philosophical Transactions of the Royal Society of London A: Mathematical, Physical and Engineering Sciences*, 210(459-470):307–357, 1911.
- [44] R. D. Richtmyer. Taylor instability in shock acceleration of compressible fluids. *Comm. Pure Appl. Math.*, 13(297), 1960.
- [45] Felix Rieper. A low-Mach number fix for Roe’s approximate Riemann solver. *Journal of Computational Physics*, 230(13):5263 – 5287, 2011.
- [46] G. Taylor. The instability of liquid surfaces when accelerated in a direction perpendicular to their planes. *Proc. Roy. Soc. (London) A*, 201:192, 1950.
- [47] B. Thornber, A. Mosedale, D. Drikakis, D. Youngs, and R. Williams. An improved reconstruction method for compressible flows with low Mach number features. *J. Comput. Phys.*, 227:4873–4894, 2008.
- [48] B. van Leer. Towards the ultimate conservative difference scheme. v-a second order sequel to Godunov’s method. *J. Comp. Phys.*, 32:101–136, 1979.
- [49] Marc Vandenboomgaerde, Claude Mügler, and Serge Gauthier. Impulsive model for the richtmyer-meshkov instability. *Phys. Rev. E*, 58:1874–1882, Aug 1998.
- [50] Yumin Yang, Qiang Zhang, and David H Sharp. Small amplitude theory of richtmyer–meshkov instability. *Physics of Fluids*, 6(5):1856–1873, 1994.